Chapter 4
Graphitic Carbon Nitride ($g\text{-}C_3N_4$)-Based Photocatalysts for Environmental Applications

Rashmi Acharya, Subhasish Mishra, Lopamudra Acharya, and Kulamani Parida

Abstract The alarmingly rising environmental pollution adversely affects the sustainable growth of modern civilization. Scientists have persistently been putting tremendous efforts over the decades to develop environment benevolent technologies to overcome this major challenge. Photocatalysis is one such technology which needs renewable solar energy and abundantly available water resources as driving forces for pollutants' degradation. In addition, the selection of an appropriate semiconductor is highly essential to degrade toxic organic compounds, hazardous heavy metals and noxious gases into harmless products efficiently. Among various semiconductor photocatalysts, $g\text{-}C_3N_4$ (GCN) is considered a robust photocatalyst because of several fascinating properties like metal-free chemical nature, visible-light-responsive activity with moderate band gap of 2.7 eV, tunable electronic structure, facile synthesis, low cost, high thermal and chemical stability. However, low surface area ($\sim$10 m^2 g^{-1}), high rate of charge carriers recombination, incomplete solar spectrum absorbance and inadequate valence band position (1.4 eV vs NHE) are some of the limitations due to which expected photocatalytic performance of GCN is yet to be achieved. Therefore, modification strategies such as exfoliating bulk GCN into nanosheets, incorporating foreign elements into its crystal structure and heterostructure formation have been employed to overcome these limitations to achieve high photocatalytic efficiency. In this chapter discusses the basic principle of photocatalytic pollutant degradation over a semiconductor surface. Recent developments in modification strategies to enhance the photoactivity of GCN have been summarised systematically. Photocatalytic applications of GCN-based photocatalysts with respect to environmental remediation are presented in this chapter. The challenges and future perspectives in designing GCN-based photocatalysts for efficient performance towards environmental applications are addressed along with the conclusion.

R. Acharya (✉) · S. Mishra
Department of Chemistry, I.T.E.R., Siksha 'O' Anusandhan Deemed to be University, Bhubaneswar 751030, Odisha, India
e-mail: drrashmiacharya75@gmail.com; rashmiacharya@soa.ac.in

L. Acharya · K. Parida
Centre for Nano Science and Nano Technology, ITER, Siksha 'O' Anusandhan Deemed to be University, Bhubaneswar 751030, Odisha, India

N. Kumar et al. (eds.), *Two-Dimensional Materials for Environmental Applications*, Springer Series in Materials Science 332, https://doi.org/10.1007/978-3-031-28756-5_4

4.1 Introduction

Recently, the world has been facing serious environmental issues and acute energy shortages due to the rapid advancement in industrialization and massive growth in the population [1]. One of the earth's most important natural resources is water, which is getting polluted day by day through the contamination of effluents containing organic dyes, antibiotics, pesticides, organic compounds and heavy metal ions [2]. For instance, various industries consume more than 100,000 commercial dyes annually. Approximately, 100 tons of dyes are discharged into waste streams per year [3]. These cause serious problems to human health, plants and aquatics owing to their acute toxicity. The need for clean water has put tremendous task for the removal of these noxious pollutants from the natural water bodies. Additionally, increased emissions containing CO_2, NO_X etc. are gradually destroying the air quality of our environment. Moreover, CO_2 level increas in the atmosphere caused by the rapid fossil fuels consumption leads to an energy crunch. This is also responsible for the global warming [4]. Several techniques like adsorption, absorption with or without chemical reaction, biological degradation and condensation have already been used to treat water [5–10]. However, several limitations have restricted these techniques for large scale applications. Therefore, an ideal technique which does not emit toxic by-products or consume much energy and possess potential to remove all kinds of pollutants, needs to be implemented [11, 12]. Advanced oxidation processes (AOPs) are considered as suitable techniques for practical application because the reactive species such as $^{\cdot}OH$, $O_2^{\cdot -}$, $SO_4^{\cdot -}$ etc., resulted from these exhibit strong redox ability to decompose almost all the water contaminants. However, most of the AOPs need large amount of chemicals and energies, which stood as the major disadvantages of the process [13, 14]. On the other hand, photocatalysis has emerged as a promising technology, which converts abundantly available solar energy into chemical energy. This technique has been applied to divergent fields including pollutant degradation, heavy metals removal, hydrogen generation, carbon dioxide conversion and organic transformations [15–18].

The concept of photocatalysis was first developed in 1972, when Fujishima and Honda produced H_2 through water splitting over TiO_2 electrode under UV illumination [19]. After this the photocatalytic technology was gradually applied in the field of environmental remediation. Carey and co-workers carried out the photocatalytic decomposition of organic pollutants by using n-type TiO_2 first in 1976 [20]. However, the expected photocatalytic performance of TiO_2 has not yet been achieved mainly due to fast rate of charge carriers' recombination and poor visible light absorptivity [21, 22]. In order to utilize visible region of solar spectrum, several visible light responsive semiconductor photocatalysts have been used for photocatalytic pollutants degradation. Among these, GCN is contemplated as a robust photocatalyst after the pioneering work of Wang and his co-workers' to produce hydrogen over it by splitting water under visible light irradiation in 2009 [23]. Carbon nitride exists in various allotropic phases such as a-C_3N_4, b-C_3N_4, GCN, cubic-C_3N_4 and pseudo-cubic-C_3N_4. Among

these, GCN is the most stable form at ambient conditions [24]. Noble GCN photocatalysts can be prepared conveniently via the facile thermal condensation of carbon and nitrogen rich precursors like ammonium thiocyanate, melamine, thiourea, cyanamide, urea and dicyandiamide [25]. The two dimensional (2D) sheets with honeycomb architecture of GCN are exist as a polymerized form of s-triazine (Fig. 4.1a) or tri-s-triazine (heptazine) units (Fig. 4.1b) as the monomers. These melon units of GCN are well connected through tertiary amine groups to form a nanosheet like structure. The so-formed nanosheets get stacked with each other by Van-der-Waals forces, which is considered as a weak force of attraction [26]. Its metal free nature, facile fabrication routes, inexpensiveness, non-toxicity, moderate band gap energy of 2.7–2.8 eV has enabled it for extensive use in solar driven photocatalysis. Moreover, the positive Valence Band level (1.4 V vs NHE at pH 7.0) the negative Conduction band position (−1.3 V vs NHE at pH 7.0) of GCN are helpful for various photoredox reactions [27–31].

However, the practical photocatalytic applications of GCN are limited mainly due to following reasons: (1) As per the density functional theory (DFT) calculations, valence band maximum (VBM) of GCN is made up of N 2p state and the conduction band minimum (CBM) is the result of hybridization between N 2p and C 2p states.

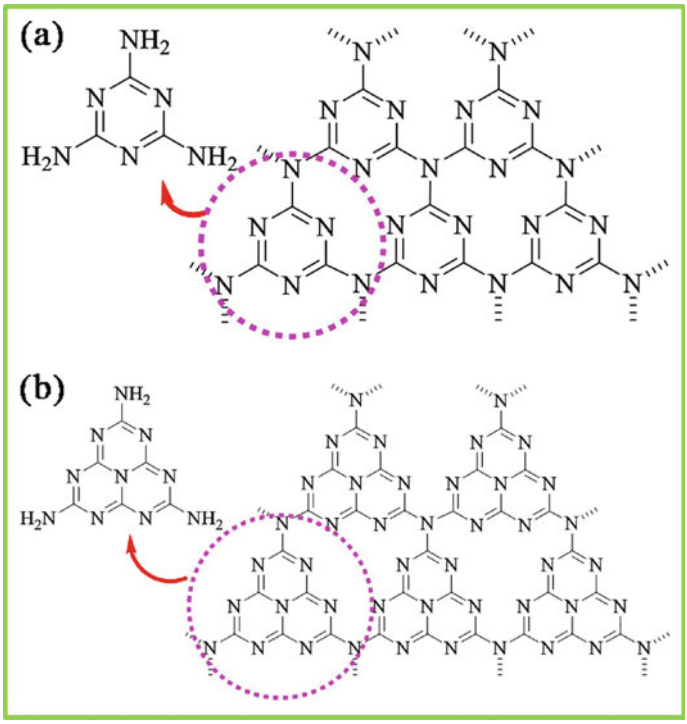

Fig. 4.1 Structure of GCN with **a** s-Triazine and **b** tri-s-triazine as building blocks. Reproduced with permission from ref. [26]. Copyright 2019, Elsevier Science Ltd.

To be precise, the photoproduced electrons distributed between the N 2p and C 2p hybridized orbitals are more vulnerable to charge carrier recombination. This process allegedly reduces the efficiency of the charge carriers and thus affects the performance of GCN as a photocatalyst (2) The band gap energy of GCN is around 2.7 eV, which corresponds to the wave length of 450 nm. Thus complete utilization of broad solar spectrum is limited. (3) It possesses weakly oxidative valence band potential of around +1.4 V, which cannot provide strong driving force to the photoinduced holes to carry out water oxidation reaction in order to generate strong reactive ·OH species required particularly for pollutant degradation. (4) The high temperature solid-phase polycondensation of organic precursors forms agglomerates of bulk GCN with relatively large size and small surface area (10–15 $m^2\ g^{-1}$) resulting in poor photocatalyic performance. (5) The difficulty in separation from treated solution also limits its practical applications [32–34].

Several modification approaches like band gap engineering, exfoliation into nanosheets and heterojunction formation with other semiconductors are implemented to augment photocatalytic activity of GCN based photocatalyts [35–37]. In this chapter, we have addressed these strategies systematically after depicting the basic principle of photocatalytic pollutant degradation over a semiconductor photocatalyst. Thereafter, divergent applications related to environmental remediation over GCN based photocatalyts were discussed. Finally, the present chapter was concluded with advantages, challenges and future perspectives of GCN based photocatalyts.

4.2 Basic Principle of Semiconductor Based Photocatalytic Pollutant Degradation

The photocatalytic pollutant degradation over a semiconductor surface usually proceeds through four important steps as presented in Scheme 4.1. Step 1 involves harvestation of light energy by the semiconductor photocatalyst (SP). The extent of light absorption depends on the textural and microstructural properties of the prepared semiconductor [38]. In step 2, electrons from the valence band (VB) of the semiconductor are excited to the conduction band (CB) by absorbing energy equal to or greater than the band gap energy (E_g) with the formation of equivalent number of holes (h^+) at the VB as shown in Eq. 4.1.

$$sp \xrightarrow{h\upsilon} h^+_{VB} + e^-_{CB} \tag{4.1}$$

Step 3 is responsible for effective migration of photoinduced charge carriers in such a way that the recombination rate of charges should be suppressed to a greater extent [39]. In step 4, the degradation of pollutants is carried out through a number of redox reactions by proper utilization of charge carriers [40]. For instance, the photoinduced electrons released from CB with adequate redox potential undergo reduction reaction with surface adsorbed O_2 molecules (ORR) to liberate reactive super oxide anions as per Eq. 4.2.

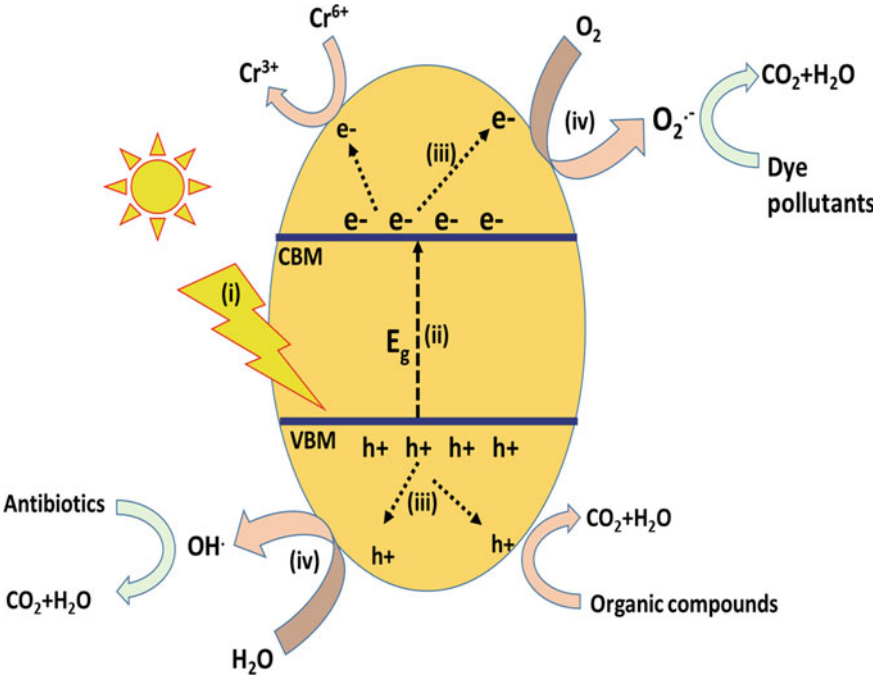

Scheme 4.1 The four step basic mechanism of semiconductor photocatalysis for pollutants removal

$$O_2 + e^-_{CB} \rightarrow O_2^{\cdot -} \tag{4.2}$$

Similarly, the surface adsorbed H_2O molecules are oxidized by the holes released from VB with desired oxidation potential to form strongly reactive ·OH radicals (Eq. 4.3).

$$H_2O + h^+_{VB} \rightarrow OH^{\cdot} + H^+ \tag{4.3}$$

These reactive species decompose the toxic organic compounds, dyes and antibiotics into harmless products (Eq. 4.4) [33]. There also appears a possibility of decomposition of these noxious substances directly by the oxidation reaction with the photoinduced holes as mentioned in Eq. 4.5 [41].

$$\text{Organic compounds/dyes/antibiotics} + O_2^{\cdot -}/OH^{\cdot} \rightarrow H_2O + CO_2 \tag{4.4}$$

$$\text{Organic compounds/dyes/antibiotics} + h^+_{VB} \rightarrow H_2O + CO_2 \tag{4.5}$$

Besides these, the photoinduced electrons are utilized to reduce CO_2 into value added products such as CH_4, CO, CH_3OH, C_2H_5OH etc. (Eq. 4.6–4.9) [42]. In addition, these electrons can be utilized for the reduction of heavy metals ions like Cr (VI), U (VI) etc. in to

$$CO_2 + 8H^+ + 8e^-_{CB} \rightarrow CH_4 + H_2O \tag{4.6}$$

$$CO_2 + 2H^+ + 2e^-_{CB} \rightarrow CO + H_2O \tag{4.7}$$

$$CO_2 + 6H^+ + 6e^-_{CB} \rightarrow CH_3OH + H_2O \tag{4.8}$$

$$2CO_2 + 12H^+ + 12e^-_{CB} \rightarrow C_2H_5OH + 3H_2O \tag{4.9}$$

their nontoxic forms (Eq. 4.10–4.11). Heavy metal ions like As (III) can be oxidized to As (V) by the photogenerated holes, $O_2^{\cdot -}$ and ·OH radicals as presented in Eq. 4.12 [18, 43, 44].

$$Cr_2O_7^{2-} + 14H^+ + 6e^-_{CB} \rightarrow 2Cr^{3+} + 7H_2O \tag{4.10}$$

$$UO_2^{2+} + 4H^+ + 2e^-_{CB} \rightarrow U^{4+} + 2H_2O \tag{4.11}$$

$$As(III) + h^+_{VB}/O_2^{\cdot -}/OH^{\cdot} \rightarrow As(V) \tag{4.12}$$

4.3 Modification Strategies for GCN

Metal free nature, facile synthesis approach, visible light responsive ability are some of the vital features that lead GCN a promising photocatalyst in diversified applications and environmental remediation in particular. However, low quantum efficiency restricts its scale up. Therefore, marvellous efforts from various quarters of researchers are made to promote its photocatalytic efficiency. Among the modification strategies, exfoliation into nanosheets, doping of foreign elements and heterojunction construction with other semiconductors are found beneficial. These strategies are depicted in this section.

4.3.1 Exfoliation of GCN

Single layer nanosheets fabricated from exfoliation of layered materials have been attracting so many eyes as a novel class of nanostructured materials [45, 46]. They possess ultrathin 2D structures in nanometer range. The quantum confinement effect thus generated from size of nanosheets contributes in upscaling the physicochemical properties [47, 48]. For instance, graphene shows extraordinary thermal, mechanical,

electrical and optical properties than its bulky counterpart, graphite [49]. In semiconductor photocatalysis, the specially designed monolayer nanosheets have numerous advantage over stacked 3D materials. The exfoliated two dimensional nanosheets possess better surface area thus have abundant number of active sites for the redox reactions to take place [50]. The bulk diffusion length of photoproduced charge carriers are also shorter in case of exfoliated sheets. Its helps in reducing the rate of recombination of charge carriers. More importantly, due to quantum confinement in nanosheets, conduction and valence bands shift in opposite directions making it a higher bandgap semiconductor [51, 52]. This helps in producing charge carriers with higher redox potential for better photocatalytic activity. Thus photocatalytic activity of bulk GCN was anticipated to enhance drastically in an exfoliated 2D nanosheet form. Taking inspiration from graphene, delamination of bulk GCN into monolayer nanosheets will be an effective strategy to improve the surface area and thus better adsorption of pollutants. Various methods including thermal, ultrasonic, chemical oxidation are used for the fabrication of GCN nanosheets. Some of the methods are disused below.

4.3.1.1 Solid State Thermal Exfoliation

The very first attempt to delaminate GCN was reported by Niu and his co-workers in 2012 via a thermal oxidation process. They prepared the nanosheets by heating bulk GCN in an open air atmosphere at 500 °C. After two hours of heating, they obtained nanosheets of ~2 nm thickness due to thermal oxidation and etching of layered material. The basic principle of this method is the hydrogen bond between the polymeric melon units get oxidized away by heating in open air from the bulk material to give exfoliated nanosheets. From the XRD plot, they reported that the peak appeared at 13.1° seemed to be less pronounced in case of GCN nanosheets. This indicated the decrease in size of the layers due to thermal oxidation. The (002) peak appeared at 27.34° shifted to 27.67° in case of nanosheets showing decreased gallery distance between the basic sheets. In comparison to bulk GCN, the nanosheets showed much higher specific surface area (SSA). From the N_2 sorption–desorption graph, they found the SSA of nanosheets was $306 m^2 g^{-1}$, whereas the bulk one has only $50 m^2 g^{-1}$. Higher SSA helps in providing more number of reactive sites to perform various reactions. They also examined the photocatalytic activity by detecting the hydroxyl (OH) radicals generated by both the bulk and exfoliated GCN. The nanosheets was observed to show better $^{\cdot}OH$ radical production [53]. Dong et al. studied the effect of temperature on the thermal exfoliation process. They prepared GCN nanosheets at different temperatures (i.e. 450, 500 and 550 °C) by heating thiourea in open air for 2 h. The sample synthesized at 550 °C was found to have better characteristics. From the SEM data they studied the textural and microstructural properties of the nanosheets prepared at different exfoliation temperature. The bulk GCN showed disorderly stalked and curved bulks with average particle size in micrometer range. Figure 4.2a shows the SEM images for sample prepared at 550 °C with several cracks over its surface. This depicted the separation between the layers and exfoliation into nanosheets of ~22 nm.

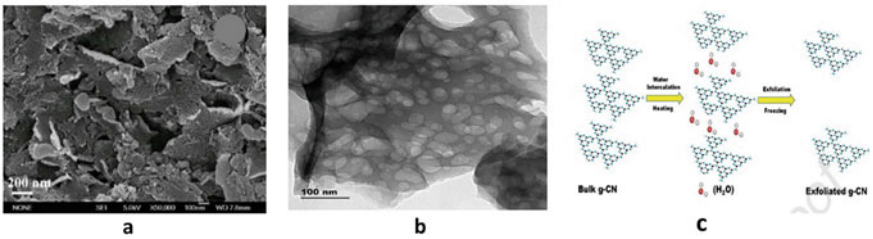

Fig. 4.2 **a** SEM micrograph for exfoliated GCN nanosheets (Reproduced with permission from ref. [54]. Copyright 2015, Elsevier), **b** HRTEM image showing plate like 2D structure of exfoliated GCN (Reproduced with permission from ref. [63]. Copyright 2019, Springer Nature), **c** Schematic diagram for bi-thermal green exfoliation of bulk GCN (Reproduced with permission from ref. [64]. Copyright 2019, Elsevier)

The specific surface area, pore volume and pore size of nanosheets were also higher than other prepared samples. They studied the photocatalytic removal of gaseous NO for each of the samples. The exfoliated GCN nanosheets were observed to perform better than the bulk one. Bulk GCN was able to remove only 18.9% of gaseous NO. Whereas, the sample fabricated at 550 °C shows a 33.5% removal efficiency [54]. They proposed a layer by layer oxidation couple mechanism with a layer splitting process for the thermal oxidation of bulk GCN into thin nanosheets. The CN layers, attached through weak van der Waals force of attraction, are constructed by polymeric melon units having weak hydrogen bonding. These bonds are too weak to stand against heavy thermal oxidation. This helps in the exfoliation of bulk GCN into nanosheets. They concluded that with increase in exfoliation temperature the size and thickness of the bulk sample get reduced.

Although, solid state thermal exfoliation process was the earliest and easiest process to synthesize nanosheets from bulk GCN, the exfoliation efficiency was low. The nanosheets formed via thermal etching constitute around 6 host layers. To synthesize single layered nanosheets, the bulk materials need to be dispersed into a solution phase. That's how the use of ultrasonic and chemical oxidation process are come into play.

4.3.1.2 Liquid Exfoliation

Ultrasound assisted methods have widely been used as a prominent liquid exfoliation method for layered materials [55, 56]. Solvent plays a vital role in ultrasonic exfoliation. When the enthalpy of mixing is minimized and solvent surface energy matches with the GCN nanoflakes, the bulk GCN starts exfoliating slowly under ultrasound [57]. Yang et al. reported an ultrasound method for liquid exfoliation of GCN by sonicating the dispersed bulk sample for 10 h. Five solvents namely methanol, isopropanol (IPA), water, N-methyl-pyrrolidone (NMP) and acetone were used separately for the purpose. The surface area of exfoliated sheets was found to be as high as $384 m^2 g^{-1}$ [58]. Still the thickness of exfoliated nanolayers was with ~ 2 nm

range which is not a unilamellar structure. Also the undispersed bulk GCN left inside the solution interferes in the exfoliation process. Thus to enhance the exfoliation efficiency and to form single layer nanosheets, chemical oxidation methods are being used. Although $KMnO_4$ was being popularly used as a strong oxidants for chemical exfoliation of layered materials, the GCN layers seems to be weakly resistant to it. Therefore mild oxidants like H_2SO_4 were chosen as a promising candidate for the chemical exfoliation process [59, 60]. Zhu and his co-workers achieved chemically exfoliated GCN nanosheets through H_2SO_4 intercalation between the host layers of GCN. The measured thickness of the GCN nanosheets was about 0.4 nm which lies very much close to the theoretically calculated value of 0.325 nm. Thus, the formation of a single layered GCN nanosheet was confirmed using a chemical exfoliation technique [61]. The H_2SO_4 assisted chemical exfoliation process was able to produce uni-lamellar GCN nanosheets with an exfoliation efficiency of nearly 60%. Yet the efficiency was still not sufficient enough. Rather, the unexfoliated and left-over particles got reassembled to form various unnecessary precipitates. This leads to deposition of sulphate in the processing solution. However, these precipitates can easily be re-dispersed in the solution via continuous water washing and complete exfoliation of GCN can be achieved using chemical methods [62].

Liquid exfoliation methods were proved to be effective for the synthesis of monolayered GCN from its bulk counterpart. Yet the use of toxic and costly chemicals is still a concern. Thus a harsh chemical free green route is necessary for the exfoliation process.

4.3.1.3 Green Exfoliation

Pattanik et al. in 2019 reported a chemical free bi-thermal route to exfoliate bulk GCN into nanosheets. The bulk sample was refluxed in water for 6 h followed by freezing for the same time interval. HRTEM images (Fig. 4.2b) showed plate like structure of exfoliated GCN sheets with d value calculated from the fringe to be 0.326 nm. This value coincided with the XRD pattern of (002) plane in exfoliated nanosheets. The specific surface area for the exfoliated nanosheets was calculated to be 63.8 m^2g^{-1}. To evaluate the photocatalytic performance of as prepared samples, degradation of ciprofloxacin was carried out. As can be expected from the SSA values, the photocatalytic degradation of ciprofloxacin was two times higher in case of exfoliated nanosheets [63]. In another work, they synthesized GCN sheets via a modified bi-thermal heating cooling cycle route. The bulk samples were refluxed in water with continuous heating and stirring for 8 h. After that, the samples were subjected to freezing for another 8 h.This heating and freezing cycles was repeated for 10 times to obtain exfoliated GCN samples. The van der Waals force of attraction between layers of bulk GCN got destructed due to continuous heating and cooling effect. Figure 4.2c shows the schematic diagram of whole synthesis process. The surface area, pore volume and peak pore size of the exfoliated sample was way much higher than the bulk one. Thus, the exfoliated nanosheets perform better photocatalytic reactions under visible light. To elucidate this, photocatalytic degradation of

Congo red (CR) was performed. The exfoliated sheet managed to decolourize 95% of the CR in the aqueous solution whereas bulk GCN was able to degrade maximum of 81.8% of CR [64].

4.3.2 Doping in GCN

The noble GCN is a polymeric nano-structured material with low band gap energy of 2.7 eV. Its appropriate band structure has drawn boundless attention of researchers in the field of photocatalysis. Additionally, the intriguing properties possessed by GCN include cost-effective, non-toxicity, earth abundance and easy preparation methods [65–67]. However, low specific surface area, minimal light absorption property and quick charge carrier recombination of GCN prevent its photocatalytic activity from being suitable for practical application [68, 69]. Hence, for the improvement of photocatalytic activity, modification processes including band gap engineering, morphology adjustment and heterojunction formation have been developed so far [70, 71]. Recently, doping i.e. introduction of impurities in to the GCN lattice has been regarded as the most effective strategy for tuning the band gap energy along with broadening the light absorption range and escalating the separation efficiency of charge carriers [72, 73]. Various metal and non-metal elements have been doped in to GCN framework in order to improve its photocatalytic activity which we have summarized in upcoming parts.

During the preparation process of metal doped GCN, the corresponding metal soluble salt is thoroughly mixed with the precursor for simultaneous doping of metal ion in to the framework of GCN [74]. However, to preserve the metal free character of GCN, non-metal element doping has attracted enormous attention of researchers. Furthermore, the existence of high ionization energy with better electronegativity, non-metal elements can generally form covalent bond by accepting electrons from the host compound [75].

Metal and non-metal doping can alter the optical and electronic behaviour, by the introduction of extra element in to framework of GCN. Besides, doped GCN can increase the separation efficiency of charge carriers, alongside improving the light absorption range and photocatalytic performance as compared to bulk GCN. Characterization techniques like PXRD, UV–Vis DRS and PL analysis have been employed to investigate the remarkable structural and optical changes of doped GCN [76, 77]. The two distinct diffraction peaks obtained in PXRD pattern of GCN are at $2\theta = 13.1$ and 27.4° correspond to (100) and (002) plane respectively [78]. The (100) and (002) plane of GCN represent the in-planar structural units of tri-s-triazine and interlayer stacking of the aromatic rings in that order [79]. As can be seen from Fig. 4.3, the increasing content of dopants resulted in the reducing peak intensity of (002) plane along with the gradual disappearance of (001) plane. This fact indicated the host-gust interaction between GCN and dopant ion hinders the crystal growth of GCN. In the PXRD pattern, no peak for dopant species has been observed although a slight shift of 2θ value to lower angle has been witnessed. This observation is

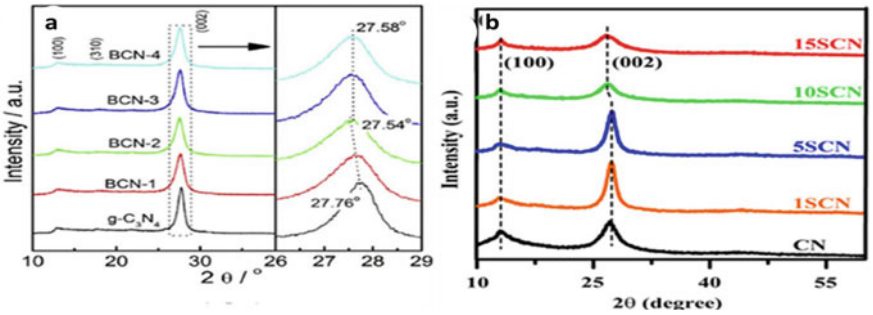

Fig. 4.3 PXRD pattern of **a** B and (Reproduced with permission from ref. [80]. Copyright 2018, Elsevier) **b** S doped GCN (Reproduced with permission from ref. [81]. Copyright 2020, Elsevier) in comparison with that of pristine GCN

ascribed to the doping of metal and non-metal ion in to the interstitial site of GCN resulting in the increase of interlayer spacing [81].

The optical properties of bulk and doped GCN are studied through UV–Vis DRS and PL analyses. Pristine GCN shows light absorption up to 460 nm. This value can be assigned to the $n\pi^*$ transition of the electron pairs present on the non-bonding orbitals of nitrogen atom and anti-bonding orbitals of the aromatic structure. In case of doped GCN, a red shift in the absorption edge to higher wavelength has been observed as shown in Fig. 4.4 [82, 83].

Moreover, the band gap energy of the doped GCN is narrowed as compared to the neat counterpart [20]. The above-mentioned results indicated the strong interaction between dopant and GCN which significantly affect the electronic arrangement and band structure of GCN. The distortion in the electronic structure strongly impacted the recombination rate of e^-/h^+ pairs. As displayed in Fig. 4.5a, doped GCN exhibits diminished PL peak intensity than that of pristine material [79, 85]. The current density of a material is highly dependent on the flow of electrons. More the number of electrons available, greater is the amount of current density [86]. Doped GCN is anticipated to exhibit improved photocurrent density in comparison to bare GCN due to its greater light absorption capacity and superior charge carrier separation efficiency. As presented in Fig. 4.5b, metal and non-metal doped GCN exhibited noticeable increased photocurrent density than that of bulk GCN [84, 87].

4.3.3 GCN/Semiconductor Heterojunction Construction

Despite the significant improvement in GCN based photocatalysis, the recombination rate of electron–hole pairs in the the semiconductor is still a major issue. Maximum amount of photoproduced electrons and holes got recombined within a few nanoseconds of their production. Thus, the photocatalytic activity is significantly reduced [88]. Formation of heterostructures with other materials could be an effective strategy

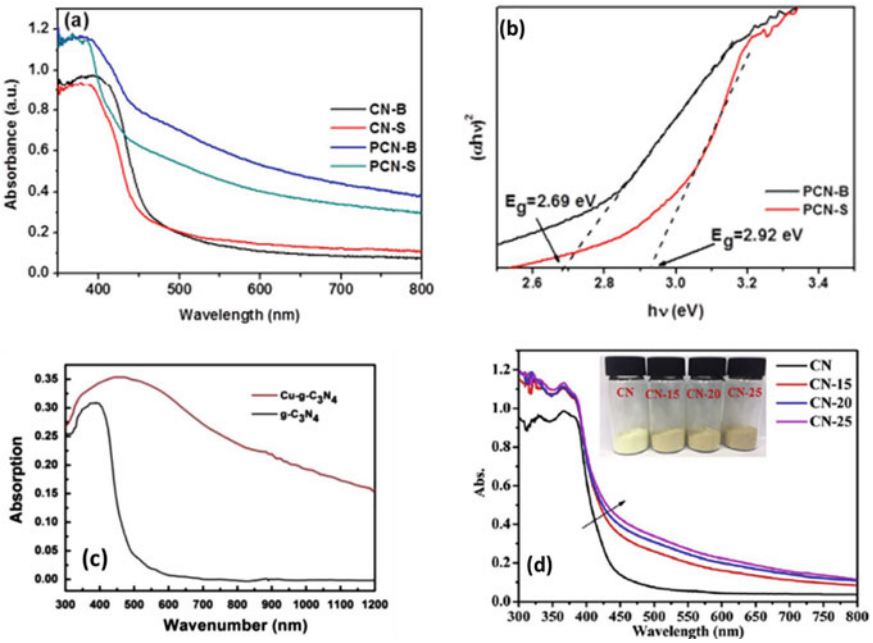

Fig. 4.4 **a** UV–Vis DRS and **b** Tauc plot for bulk (CN-B), exfoliated (CN-S), P- doped GCN (P-CN) and P-doped exfoliated (P-CNS) GCN (Reproduced with permission from ref. [82]. Copyright 2017, Elsevier), **c** solid state UV–vis–NIR diffuse reflectance spectra of GCN and Cu doped GCN (Reproduced with permission from ref. [83]. Copyright 2015, Elsevier) **d** UV- vis DRS of GCN samples prepared with different N ratios. Reproduced with permission from ref. [84]. Copyright 2016, Elsevier Science Ltd.

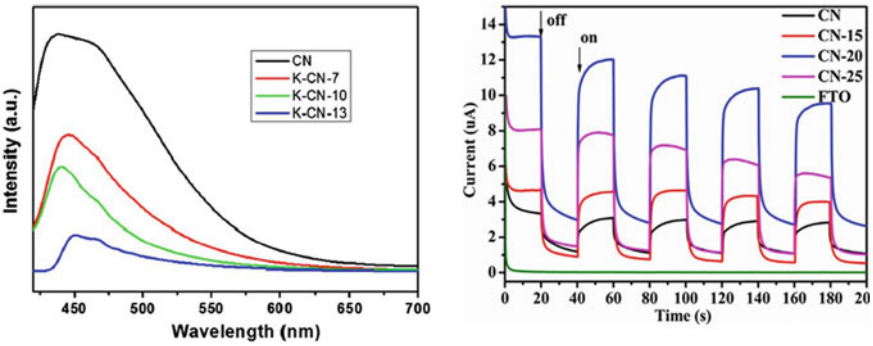

Fig. 4.5 **a** Photoluminescence spectra of k doped GCN (Reproduced with permission from ref. [85]. Copyright 2018, Elsevier) and **b** Transient photocurrent plots of **a** N doped GCN. Reproduced with permission from ref. [84]. Copyright 2016, Elsevier Science Ltd.

to improve the life span of charge carriers. Heterojunction is basically the contact of interfaces between two semiconductors with different band gaps. Formation of GCN heterostructures can significantly be supressed the recombination rate by effective spatial separation of charge carriers across the heterojunction interface. Heterojunction not only enhances the lifetime of charge carriers, but also the light absorption range, band positions and improved surface reactions. These augmented properties finally lead to better photocatalytic performance of pristine GCN. Construction of heterojunctions is considered as most feasible and effective strategy to increase the photocatalytic activity to many folds [89–92].

However, not every material can form a heterojunction with the pristine GCN. The bandgap and band position of both the semiconductor plays a vital role in the formation of coupling hybridization across the interface [93]. The difference in chemical potential between both the semiconductors created band bending in the interface. This bending leads to the movement of charge carriers in opposite directions creating a built in electric field. This effect helps in limiting the recombination by enhancing the spatial separation of electrons and holes [94, 95]. The difference between the lattice spacing of two semiconductor creates a lattice mismatch which can further leads to formation of defects in semiconductor. These defect help in trapping the electrons and thus reduces the diffusion of photoproduced charges. Thus formation of heterostructure was anticipated to be an effective way to upscale the photocatalytic activity of pristine GCN. Various attempts was made to couple pristine GCN with different materials such as CdS, ZnO, TiO_2, BiOI etc. [96–100]. Some of the novel works on GCN based heterostructures are discussed below.

Li et al. fabricated GCN coupled TiO_2 composites via a simple sol–gel process for augmented photodegradation of methyl orange (MO) under UV and visible light irradiation. The XRD patterns for the composites with different weight percentage of GCN are shown in Fig. 4.6a. The peaks of GCN, TiO_2 and the composites coincided well with each other for every prepared composite sample. This indicated the formation of heterojunction between both the nanomaterials. The prepared composite was tasted to perform better photocatalytic activity than the pristine counter parts. TiO_2, owing to its higher bandgap is a UV light active material, whereas the composite was able to generate photoproduced electrons and holes under visible light irradiation. This suggested that the red shifting in the absorption range of TiO_2 is due to the formation of heterojunction with GCN. Subsequently, TiO_2 was unable to degrade MO under visible light whereas the composite showed maximum of ~80% MO degradation owing to better light absorption and spatial separation of photoproduced electron and hole pairs. [101]. A 3D GCN /TiO_2 photocatalyst composite was prepared by Sheng et al. from TiO_2, melamine and ciyanuric acid using a one-step calcination method. From the HRTEM images shown in Fig. 4.6b, a good contact between GCN and TiO_2 can be observed. The thin GCN nanosheets were coated well over the surface of TiO_2. The TiO_2 nanoparticle showed a clear and regular lattice fringe of width 0.35 nm. The photocatalytic activity of the pristine samples and composite were compared by degrading methylene blue (MB) and phenol. The composite exhibited better charge transfer and spatial separation. This leads to the

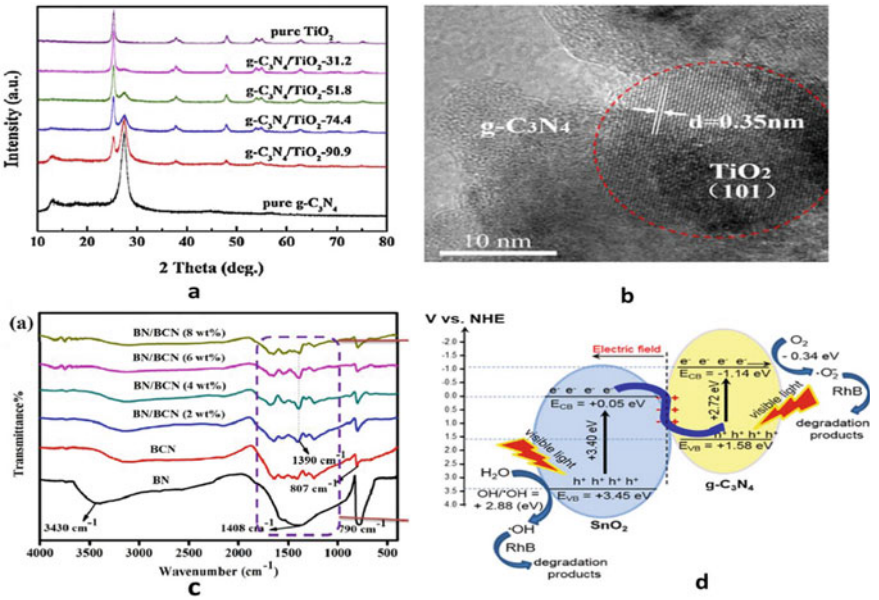

Fig. 4.6 **a** XRD plots for GCN, TiO_2 and GCN/TiO_2 composites (Reproduced with permission from ref. [101]. Copyright 2016, Elsevier), **b** HRTEM images 3D GCN/TiO_2 composite (Reproduced with permission from ref. [102]. Copyright 2019, Elsevier), **c** FTIR spectra of BN, BCN and BN/BCN composites (Reproduced with permission from ref. [86]. Copyright 2020, Elsevier), **d** Schematic illustration of S-scheme charge transfer path between SnO_2 and GCN (Reproduced with permission from ref. [106]. Copyright 2022, Elsevier)

generation of more amount of hydroxyl (·OH) radicals and thus shows better photocatalytic activity. The composite shows 4 and 4.5 times enhanced degradation of MB and phenol degradation respectively [102].

Construction of p–n heterojunction is also another remarkable method to enhance the photogenerated charge separation of GCN. Tian et al. fabricated a Cu_2O/GCN p-n heterojunction by depositing Cu_2O over GCN surface. Owing to the narrow band gap energy of Cu_2O, the optical absorption of GCN was enhanced in the visible region of solar spectrum. Thus, an augmented photocatalytic performance was observed in case of Cu_2O/GCN p-n heterojunction [103]. In another work. Acharya et al. synthesized a boron nitride/B-doped-g-C_3N_4 (BN/BCN) hetertojunction for the degradation of tetracyclin hydrochloride (TCH) in aqueous environment. They prepared the composites with different weight ratios of BN via an in-situ growth process. From the FTIR peaks presented in Fig. 4.6c, the strong bonding within BN and BCN can be easily predicted. The in-plane B-N stretching band at 1408 cm^{-1} got shifted to a higher frequency of 1390 cm^{-1}. With the increase in amount of BN, the intensity of peak formed at 1390 cm^{-1} for the composite increased. These observations from the FTIR spectrum confirmed the formation of heterojunction between BN and BCN. The photocatalytic TCH degradation ability of the as prepared composite was

higher than the pristine counterparts. They calculated the rate constant (k) value for the degradation of TCH via different samples. The sample with 4wt% of BN shows maximum activity under sunlight. The k value for BCN sample was 9×10^{-3} min^{-1} whereas for BN/BCN (4 wt%), the value was increased to 34×10^{-1}. These values interpreted the enhancement in photocatalytic activity of GCN through construction of nano-heterojunction with Z-scheme charge transfer mechanism [86].

Fu et al. reported a 2D-2D WO_3/GCN step scheme (S- scheme) hetrostructured composite fabricated through electrostatic self-assembly method. The band positions and composition of the prepared composite was measured by density functional theory (DFT). From the computational calculations, they discovered that the charge transfer across the heterojunction is affected by the difference in work function and fermi levels of the participating semiconductors. The calculated work function of WO_3 was 6.23 eV whereas that for GCN was 4.18 eV. As WO_3 possess a higher work function value, the electrons starts flowing from the surface of GCN to WO_3 until a fermi level equilibrium was established. Due to this charge transfer process, a built in electric field was produced at the heterojunction interface between GCN and WO_3. This helps in enhancing the transfer and separation of charge carrier across the heterojunction interface eventually leading to augmented photocatalytic activity. In this case, the composite performed 1.7 times better photocatalytic H_2 production than that of pristine GCN [104].

Another S scheme based GCN /Bi_2MoO_6 heterostructure was constructed by Zhen et al. The water dispersed Bi_2MoO_6 mixed with GCN was treated under different calcination temperature to form the composite. The composite was proved to be more effective than pristine GCN in photodegradation of phenol under visible light irradiation [105]. Recently, Van et al. reported a SnO_2/GCN system from annealing mixture of SnO_2 and GCN for the photodegradation of Rhodamine B (RhB). The suggested S-scheme charge transfer path between both the nanomaterials is depicted in Fig. 4.6d. From the figure, it can be seen that the electrons and holes produced on the CB of SnO_2 and VB of GCN respectively get recombined due to equivalent band positions and fermi level alignments. The unwanted charge carriers got recombined to give a better separation of useful charge carriers. This mechanism escalates the photodegradation of RhB under visible light irradiation [106].

4.4 Environmental Remediation Through Photocatalytic Technology

4.4.1 Photocatalytic Degradation of Organic Compounds, Dyes and Antibiotics

The rising concentration of organic compounds, dyes and antibiotics in aqueous environment has received great attention in recent years [107]. The photocatalytic degradation of these pollutants using GCN based materials has been found advantageous

over the conventional treatment methods. It was observed that modified GCN photocatalysts exhibited enhanced phocatalytic performance for pollutant degradation in comparison to pristine one. Pattnaik et al. reported that about 95% of Congo red (CR) was degraded by exfoliated GCN whereas the bulk GCN degraded only 81%. The enhanced photoactivity of exfoliated GCN might be due to its porous nature. The suggested mechanism of degradation was shown in Fig. 4.7. According to it, $^{\cdot}O_2^-$ and $^{\cdot}OH$ are the prime reactive species which were confirmed from the scavenging tests for the enhanced degradation of CR. These are produced as per the following equations [64].

$$e - \text{GCN} \xrightarrow{hv} e_{\text{CB}}^- + h_{\text{VB}}^+ \tag{4.13}$$

$$\text{e}_{\text{CB}}^- + \text{O}_2 \rightarrow {}^{\cdot}\text{O}_2^- \tag{4.14}$$

$$e_{\text{CB}}^- + {}^{\cdot}\text{O}_2^- + 2h_{\text{VB}}^+ \rightarrow \text{H}_2\text{O}_2 \tag{4.15}$$

$$\text{e}_{\text{CB}}^- + \text{H}_2\text{O}_2 \rightarrow {}^{\cdot}\text{OH} + \text{OH}^- \tag{4.16}$$

$$\text{CR} + {}^{\cdot}\text{OH} \rightarrow \text{H}_2\text{O} + \text{CO}_2 \tag{4.17}$$

$$\text{CR} + {}^{\cdot}\text{OH} \rightarrow \text{H}_2\text{O} + \text{CO}_2 \tag{4.18}$$

Or.
The overall reaction may be presented as

$$\text{CR} + {}^{\cdot}\text{OH} + {}^{\cdot}\text{O}_2^- \rightarrow \text{H}_2\text{O} + \text{CO}_2 \tag{4.19}$$

In another study, Pattnaik et al. observed an enhanced photodegradation of ciprofloxacin (CPN) over exfoliated GCN under solar light irradiation. They observed that 78% of 20 ppm CPN was degraded in 1 h by 1gL^{-1} of exfoliated g-C_3N_4. The augmented performance of exfoliated GCN might be attributed to its extremely large surface area and low recombination rate of photogenerated charge carriers [63].

Harraz and co-authors demonstrated the superior performance of Au doped GCN in the photodegradation of methylene blue (MB). The photodegradation rate of the 1%Au/g-C_3N_4 nanocomposite was found to be 2.69 times higher than that of bare GCN [108]. Yan et al. reported that B doped GCN (BCN) exhibited promoted RhB decomposition [109]. Recently, Acharya et al. demonstrated the enhanced performance of exfoliated BCN (eBCN) over BCN in photocatalytic removal of CPN. The degradation efficiency of eBCN was about 1.2 times more than that of bulk BCN. The increased degradation rate was ascribed to the excellent photoinduced charge carriers' separation which was confirmed from the high photocurrent density of 524 mA cm^{-2} displayed by e-BCN [66].

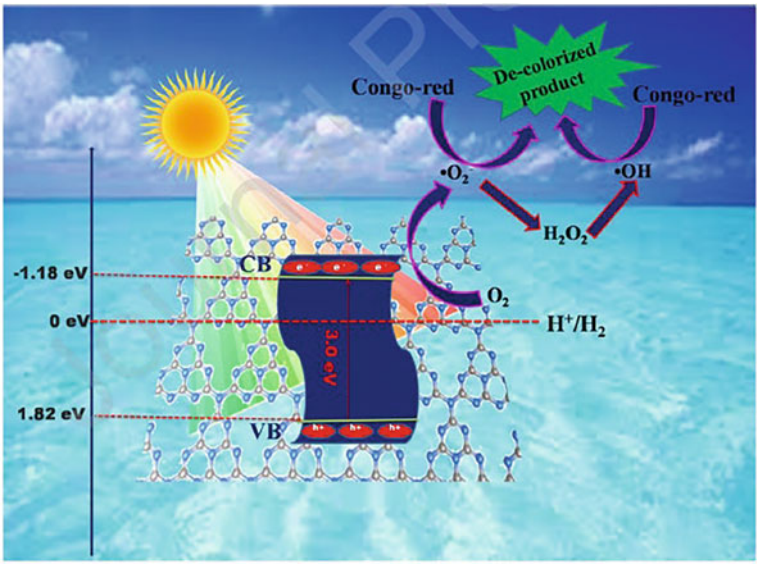

Fig. 4.7 Pictorial presentation of reaction mechanism for degradation of CR over e- GCN under sun light. Reproduced with permission from ref. [64]. Copyright 2019, Elsevier Science Ltd.

Wu group have developed 2D-2D TiO_2/GCN heterostructured nanocomposite for the removal of methyl orange (MO). The face-to-face heterojunction exhibited an improved flat potential, and decreased band gap energy with adequate change in band positions which are found advantageous for promoting charge mobility across the interface, lowering charge transport distance and time. These cumulatively enhanced the photodegradation rate (0.189 min^{-1}) of MO under UV–visible light [110]. Wang et al. constructed a robust GCN/Nb_2O_5 heterojunction through a direct electrospinning route followed by calcination. They observed that niobium pentoxide nanofibers (Nb_2O_5 NFs) were tightly bound onto GCN nanosheets which facilitated a promoted charge carriers' transfer. As a result, the heterostructured photocatalyst showed a remarkable performance in the degradation of phenol and RhB under visible light irradiation. Charge carriers trapping experiments revealed that holes (h^+s) and superoxide radical anions ($\cdot O_2^-$s) were the principal reactive species in the degradation process. The suggested mechanism for organic pollutants' photodegradation is depicted in Fig. 4.8 [111].

Acharya et al. have proposed a type-II p-n heterojunction with Z-scheme charge transfer mechanism for BN/BCN composite photocatalyst in which p-type BCN nanosheets were well covered with n-type born nitride (BN) particles. The heterostructured photocatalyst containing 4 wt. % of BN performed 88% tetracycline (TCH) degradation under solar light irradiation at time period of 60 min. superoxide ($^{\cdot}O_2^-$) and hydroxyl (OH^-) radicals were found as the major reactive species for TCH removal. The suggested mechanism of TCH degradation is illustrated in Fig. 4.9 [86].

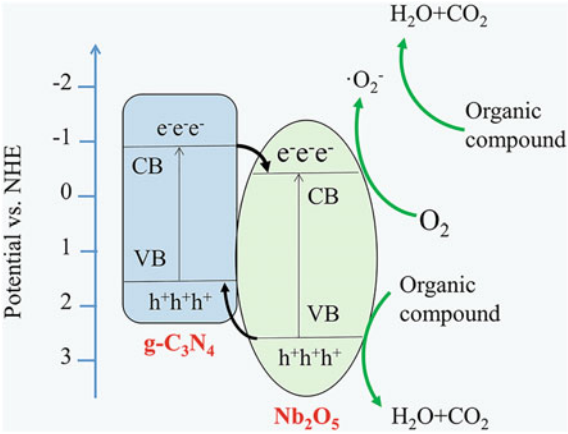

Fig. 4.8 Schematic diagram of photogenerated charges in GCN/Nb_2O_5 heterojunction (Reproduced with permission from ref. [111]. Copyright 2021, Nature)

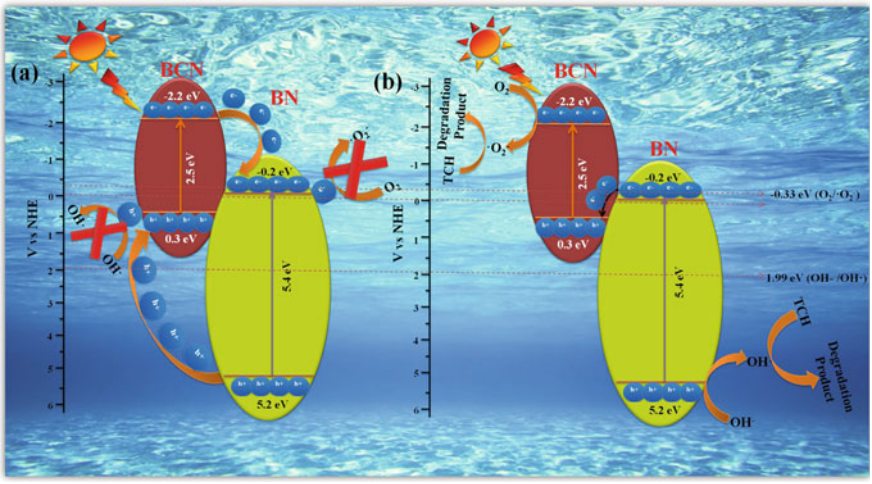

Fig. 4.9 Scheme showing charge transfer mechanism for TCH degradation over BN/BCN composite. Reproduced with permission from ref. [86]. Copyright 2020, Elsevier Science Ltd.

4.4.2 Photocatalytic CO_2 Conversion

The prime product of fossil fuels' combustion is CO_2, which causes greenhouse effect when released into the atmosphere. Conversion of it into selective hydrocarbon-based energy fuels and chemicals is considered as an effective method for CO_2 recycling which is identical to nature's carbon cycle [112–114]. Different types of gaseous/liquid products can be obtained from CO_2 through multiple electron transfer

mechanisms as it is the highest oxidation state of carbon. Various reduction products of CO_2 and their standard reduction potential of formation was enumerated in Table 4.1 [42]. It was evident that these are located near the H_2O reduction potential. Therefore, the materials used for solar water splitting can also be used for CO_2 reduction [115]. The main demerits in CO_2 conversion are its high chemical stability and inertness owing to its linear structure with high C = O double bond energy (>750 kJ mol^{-1}) [116, 117]. However, photocatalytic reduction of CO_2 into green solar fuels like methanol (CH_3OH), methane (CH_4), formaldehyde (HCHO) and formic acid (HCOOH) has been recognized as a promising technology as CO_2 level can be imitated in the atmosphere with simultaneous production of useful chemicals and solar fuels [118–120]. The first CO_2 reduction by PEC into CH_3OH, HCOOH, and HCHO using p-GaP photocathode and carbon anode was carried out by Halmann [121]. Since then numerous studies have been reported on photocatalytic CO_2 conversion into value added products [122–124].

Photocatalytic CO_2 degradationtion process mostly relies on the ability of the catalyst to adsorb chemical rection intermediates over its surface. To do the same, the prepared photocatalyst had to have enhanced surface properties and adequate number of surface active sites than its pristine counter parts. Surface properties $SnFe_2O_4$ (SFO)/GCN Z-scheme heterojunction was compared with that of SFO and GCN. From the BET surface area analysis, the specific surface area of $SnFe_2O_4$, GCN and the composite was found to be 11.42, 15.11, and 44.41m^2/g respectively. The incorporation of GCN into the ferrite system enhances the specific surface area to a great extent. These analysis depicted that enhanced surface area and porous structure of the composite helps in better adsorption of CO_2 and other reaction intermediated over the surface active sites. The CO_2 adsorption curves for SFO, CN, and SFO-CN

Table 4.1 Various reduction products of CO_2 their standard reduction potential of formation with equation

Sl no	Name of the product formed	Standard reduction potential (E_0) versus NHE at pH 7	Chemical equation for formation
1	CH_4	−0.24	$CO_2 + 8\,h^+ + 8e^- \rightarrow CH_4 + 2H_2O$
2	CH_3OH	−0.38	$CO_2 + 6\,h^+ + 6e^- \rightarrow CH_3OH + H_2O$
3	HCHO	−0.48	$CO_2 + 4\,h^+ + 4e^- \rightarrow HCHO + H_2O$
4	CO	−0.52	$CO_2 + 2\,h^+ + 2e^- \rightarrow CO + H_2O$
5	HCOOH	−0.61	$CO_2 + 2\,h^+ + 2e^- \rightarrow HCOOH + H_2O$
6	C_2H_4	0. 06	$2CO_2 + 12\,h^+ + 12e^- \rightarrow C_2H_4 + 4H_2O$
7	C_2H_5OH	0.08	$2CO_2 + 12\,h^+ + 12e^- \rightarrow C_2H_5OH + 3H_2O$

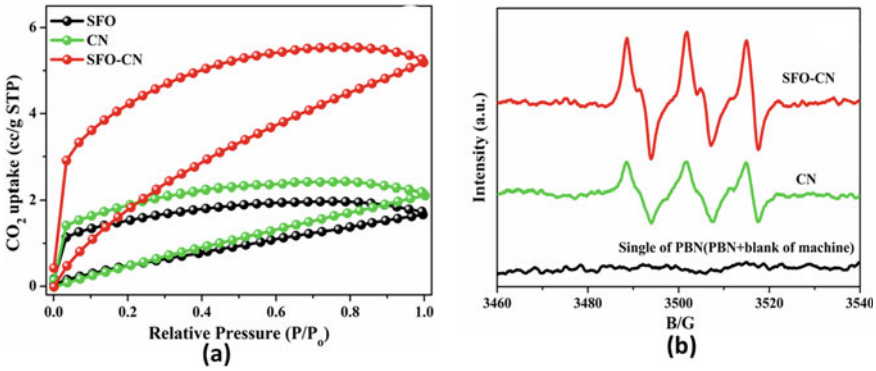

Fig. 4.10 **a** CO_2 adsorption curves **b** the profiles of ESR signal of the radicals in the reaction. Reproduced with permission from ref. [125]. Copyright 2020, Elsevier Science Ltd.

were displayed in Fig. 4.10a. At P/P0 = 1.0, the CO_2 adsorption ability of SFO, CN, and SFO-CN is 1.67, 2.11, and 5.19ccg^{-1} respectively. Figure 4.11a indicated that the SFO-CN with larger pore volume and surface area possessed greater CO_2 adsorption ability [125].

Generally, CO_2 absorbed in the surface active sites is reacted with hydrogen ions and electrons to produce $^{\cdot}CO^{2-}$, which is considered as a key intermediate for the production of CO [126, 127]. The strong signal intensity of the $^{\cdot}CO^{2-}$ radicals in the Electron spin resonance (ESR) spectra of SFO-CN observed in Fig. 4.10b. For SFO-CN demonstrated that release of more number of $^{\cdot}CO^{2-}$ species for efficient reduction CO_2 to CO. In fact, the $SnFe_2O_4$/GCN composite showed 2.2 times higher CO evolution than the pristine CN. The CO evolution value for the CO_2 photodegradation for the composite and pristine GCN was 7.56 and 3.45 μmol/g/h respectively [125].

Li et al. investigated kinetically selective CO production over GCN/Bi_2WO_6. The composite photocatalyst with Z-Scheme heterostructure exhibited an enhanced CO production rate of 5.19 μmol g^{-1} h^{-1} under visible light illumination [128]. According to Sonowal et al., the coupling of GCN quantum dots (GCNQDs) with Zr (IV) MOF resulted a binary composite which yielded methanol of 386 $\mu mol.h^{-1}.g^{-1}$ through photocatalytic reduction of CO_2. On the other hand the pristine MOF produced only 66 $\mu mol.h^{-1}.g^{-1}$. The superior performance of the composite is due to the synergistic effect of GCNQDs, which makes photoinduced electrons available abundantly on the surface of the composite photocatalyst by prominent separation of charge carriers. These electrons selectively reduce CO_2 to methanol [129].

4.4.3 Photocatalytic Removal of Heavy Metal Ions

Heavy metal ions such as Cr (VI), U (VI), As (III), Hg (II) etc. are acutely toxic and are major pollutants in industrial effluents. These cannot be easily degraded in to

harmless products unlike organic pollutants and get accumulated in living organisms to cause serious health hazards. Therefore, it has recently been a major challenge to decontaminate these noxious metal ions in order to protect the human health and the environment in particular [130]. Several technologies including solvent extraction, adsorption, chemical precipitation, electrocoagulation, photocatalysis, oxidation/reduction, ultra-filtration, reverse osmosis etc. have been developed for the elimination of these toxic metal ions from aqueous environment [131]. Among these, photocatalysis is considered as a well acclaimed process owing to a number of advantages like conversion of metal ions into nontoxic forms, use of abundantly available solar energy, reusability and low cost [132, 133]. Photocatalytic detoxification of these metal ions was depicted in the following sections.

4.4.3.1 Photocatalytic Reduction of Cr (VI)

As a corrosion inhibitor chromium is widely applied in various industries like dye synthesis, leather tanning, refractories, electroplating, alloy and steel manufacturing. The effluents of these industries containing Cr (VI) usually range up to 500 ppm. The improper disposal and accidental leakage at industry sites also contributes to the Cr (VI) contamination. Besides this, natural oxidation of the Cr (III) of ophiolitic rocks and ultramafic derived soils produce some amount of Cr (VI). It is acutely toxic, carcinogenic, teratogenic and mutagenic in biological systems. The nonbiodegradable and bioaccumulative properties of Cr (VI) allow it to pass through the cell membrane. Then, these are reduced to Cr (III) with the help of reactive oxygen species (ROS) causing intracellular damage. The so formed Cr (III) ions form stable coordination complexes with proteins and nucleic acids. This results in genotoxic damage and other forms of toxicity [9].

Cr (VI) exists as different oxy anionic species in aqueous medium depending on the concentration and pH of the solution. For instance, the dominating species is H_2CrO_4 at pH below 1.0 while $HCrO^{4-}$ and $Cr_2O_7{}^{2-}$ are the predominating species between the pH 1.0 and 6.0. $CrO_4{}^{2-}$ is the stable species above pH 6.0. These oxyanionic species experience repulsion from soil particles carrying negatively charges. As a result, these are passed easily into the aquatic environment and pose threat to aquatic bodies as well as downstream users. Owing to the hazardous impact, the maximum permitted Cr (VI) limit in surface and drinking water was mandated as 0.1 and $0.05 mgL^{-1}$ respectively by the USEPA [134]. In order to minimize the detrimental impact of Cr (VI) on downstream users and aquatic lives, it is essentially required to reduce the concentration below the permissible level before its discharge into the aquatic environment. Conversion of Cr (VI) to Cr (III) is a suitable approach for minimizing Cr toxicity as the latter is about 1000 times less toxic and is an essential nutrient for living organisms. Moreover, it is highly stable, less mobile in aqueous environment and can easily be precipitated as Cr $(OH)_3$ making the separation process easier [4]. Although, chemical precipitation, electrochemical reduction, sulphide precipitation have been adopted for detoxification of Cr (VI), large number

of bottlenecks in these processes restrict their applications. On the other hand, photocatalytic reduction Cr (VI) into Cr (III) is considered as an effective, inexpensive and environmentally benevolent technique [33]. Therefore, several researches have been highlighted on these aspects.

Wang et al. prepared Br-doped GCN in which N atoms are substituted by Br atoms without destroying the original GCN framework. The incorporation of Br widened the light response to 800 nm along with the enlargement in surface area and promotion in charge carriers' separation efficiency. As a result Br-GCN experienced an enhanced Cr (VI) reduction rate which was found two times more than that obtained by bare GCN [135]. A CoS_2/g-C_3N_4-rGO hybrid nanocomposite was synthesized by a simple one-pot solvothermal technique. The heterostructured composite reduced 99.8% of Cr (VI) within 120 min at pH = 2 under visible light irradiation. Further, the photoreduction efficiency for the composite was more than 98% after 5 consecutive cycles. The enhanced performance might be attributed to increase in visible light utilization, high surface area and prominent electron–hole pairs separation which are due to formation a heterostructure [136].

4.4.3.2 Photocatalytic U (VI) Reduction

Uranium appears as U (0), U(III), U(IV) and U(VI) states among which U(VI) soluble and U(IV) is sparingly soluble [137]. It is extensively used in nuclear industries. The insufficient processing of spent fuel releases large amount of uranium into the environment. It has been reported that uranium emissions in excess leads to serious environmental pollution. Various methods like adsorption, ion exchange, evaporation and ultrafiltration are used for the treatment of U(VI) [138]. These processes have certain shortcomings due to which a green, efficient, and highly selective technology should be developed for remediation of U (VI). Photocatalytic reduction of soluble U (VI) to insoluble U (IV) can be regarded as advantageous technique. It is predicted that photoreduction of U (VI) takes place in two different ways. First is reduction of U (VI) through single-electron reduction process as shown in Eq. 4.20, U (VI) so formed in the above step is further reduced to U(IV) according to Eq. 4.21 [139].

$$\mathrm{U(VI)} + e^-_{\mathrm{CB}} \rightarrow \mathrm{U(V)} \tag{4.20}$$

$$\mathrm{U(V)} + e^-_{\mathrm{CB}} \rightarrow \mathrm{U(IV)} \tag{4.21}$$

In the second case, U(VI) is reduced directly to U (IV) by two electrons in acidic medium as presented in Eq. 4.22 [140].

$$\mathrm{UO_2^{2+}} + 4\mathrm{H^+} + e^-_{\mathrm{CB}} \rightarrow \mathrm{U^{4+}} + 2\mathrm{H_2O} \tag{4.22}$$

It was reported that the standard reduction potentials of $UO_2{}^{2+}/U^{4+}$, $UO_2{}^{2+}/UO_2$ and U_4O_9/UO_2 redox couple are 0.267, 0.411 and 0.456 V, respectively [141]. This

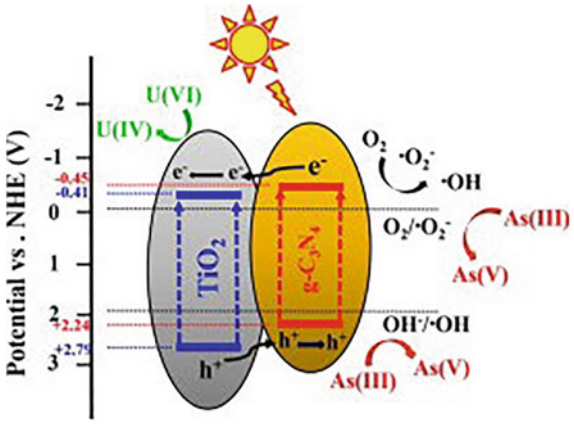

Fig. 4.11 Mechanism of simultaneous U (VI) photoreduction and As (III) photooxidation over GCN/TiO_2 heterostructured photocatalysts. Reproduced with permission from ref. [144]. Copyright 2018, Elsevier Science Ltd.

suggested that GCN based photocatalysts with more negative CB potentials can easily reduce U(VI). In 2016, Lu et al. synthesized boron doped GCN (BCN) for photocatalytic reduction of U (VI) under visible light irradiation in presence of methanol as a hole scavenging agent. The photogenrated electrons (e^-_{CB}s) are used to reduce U (VI) to insoluble U (IV) whereas the photogenerated holes (h^+_{VB} s) oxidize methanol to CO_2 and H_2O [142]. Chen et al. reported that g-C_3N_4/graphene oxide nanosheets (GCN/GO) exhibited 100% U (VI) removal efficiency after five cycles [143]. Jiang et al. investigated the simultaneous reduction of U (VI) and oxidation of As (III) over GCN/TiO_2 heterostructured photocatalysts under simulated solar light illumination. They observed that maximum of 83% UO_2^{2+} is reduced in 240 min. As per the proposed mechanism shown in Fig. 4.11, $O2^{\cdot-}$, ·OH and h_{VB}^+ were the main active species for As (III) oxidation and U (VI) was reduced with the help of e_{CB}^- [144].

4.4.3.3 Photocatalytic Oxidation of as (III)

The two most stable state of Arsenic is As (V) and As (III). As (V) exist as $H_2AsO_4^-$ and $HAsO_4^{2-}$ species while H_3AsO_3 is the common species of As (III) at neutral pH [145, 146]. It has been reported that toxic effect of As (III) is about 26–60 times more than that of As (V) [147]. Therefore, the World Health Organization (WHO) has mandated 10 mg L^{-1} as the maximum permissible limit of arsenic in drinking water [148]. Water pollution caused by As (III) has been a challenge due to its non-biodegradability as well as accumulative property in food chain [149]. Although several methods including ion exchange, adsorption, chemical oxidation and precipitation are developed, chemical oxidation technique is considered as an effective approach. Oxidizing agents like O_3, MnO_2, Cl_2, $NaClO_7$ and MnOOH are efficiently used to remove As (III). However, these consume more energy and cause secondary pollution. On the other hand, photocatalysis is relatively cheaper and environmentally friendly for the detoxification of As (III) [150, 151]. Ouyang

et al. synthesized boron-doped black TiO_2/GCN nanocomposite by sol−gel process followed by in situ decomposition-thermal polymerization technique. The obtained composite exhibited a promoted As (III) photo-oxidation to As (V). Electron spin resonance (ESR) and the radical scavenging experiments evidenced that hydroxyl radicals, superoxide anions and holes synergistically participated to oxidize As (III) [152]. A Mineral-based bentonite/GCN 2D-2D composite was prepared by a self-assembly process. The incorporation of bentonite resulted in enhanced surface area and pronounced excitons' separation. As a result, the prepared photocatalyst showed three times higher photooxidation of As (III) than that exhibited bare GCN. Additionally, high efficiency in As (III) photooxidation was also displayed in a wide pH range from 3 to 8.5. It was observed from ESR and radical trapping tests that $^{\cdot}O_2$ species is the prime reactive species for the oxidation of As (III) [153].

4.4.3.4 Photocatalytic Reduction of Hg (II)

Various industries like rubber processing, chloralkali, oil refining, paint, fertilizer manufacturing etc. releases Hg to the aquatic environment in form of effluents. It is converted to methyl mercury by bacteria. This organic mercury being non-biodegradable and bio- accumulative in nature, easily enters into the food chain [154]. As it is acutely toxic, introduction of this deadly pollutant in form Hg (II) causes serious detrimental impact on important organs like brain, liver, reproductive system etc. [155]. Therefore, Hg (II) is being received great attention as an acute pollutant for the last several decades and US-EPA has fixed ~2 μg/L as its maximum permissible limit in drinking water [156]. Therefore, adsorption, electrodeposition, co-precipitation and heterogeneous photocatalytic reduction are some of approaches that are practiced for removal of Hg (II) ions [157]. However, photocatalytic reduction of Hg (II) is recently gaining importance owing to its several advantageous features like use of abundantly available water resources and solar energy [158]. Alshaikh et al. reported that $CuAl_2O_4$/g-C_3N_4 nanostructured photocatalysts prepared by MCM-41 and F-127 assisted solution process, exhibited enhanced photoactivity towards reduction of Hg (II). The highest Hg (II) photoreduction rate of 189.4 μmol min^{-1} was observed for 3.0 wt% $CuAl_2O_4$-decorated GCN whereas pristine GCN and $CuAl_2O_4$ displayed a poor performance of 21.95 and 12.95 μmol min^{-1} respectively. The enhanced rate of Hg (II) photoreduction was attributed to formation of a robust heterojunction which minimized the charge carriers' recombination rate and reduction in band gap energy [159]. Mohamed and Ismail constructed a p-n heterojunction between mesoporous $BiVO_4$ NPs and GCNnanosheets through a simple soft and hard template-assisted approach. The synthesized nanocomposites possessed enlarged surgace area with improved crystanility. They proposed Z-Scheme charge transfer route for the photocatalytic reduction of Hg (II) as presented in Fig. 4.12 Maximum of 100% Hg (II) photodegradation was observed by 1.2% $BiVO_4$/GCN nanocomposite in 60 min. The observed reduction efficiency was found to be 3.9 time more than $BiVO_4$ NPs and 4.5 times larger than that of pristine GCN [160].

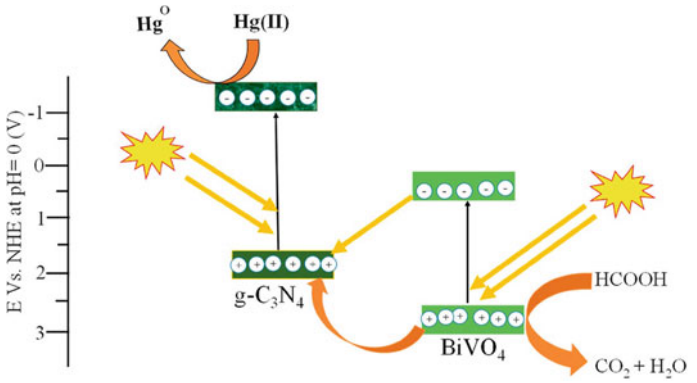

Fig. 4.12 Photocatalytic reduction of Hg (II) over mesoporous $BiVO_4$/GCN nanocomposites through Z-scheme charge transfer process. Reproduced with permission from ref. [160]. Copyright 2021, Elsevier Science Ltd.

4.5 Conclusion and Outlook

In summary, the present chapter highlights the basic mechanism for photocatalytic degradation of pollutants and modification strategies of GCN for enhanced photocatalytic pollutant degradation. Obviously, GCN has proven to be a promising candidate for modification and the modified forms have shown excellent performance for environmental remediation. Therefore, the growth of modified GCN based photocatalysts will be accelerated in near future to eradicate pollutants from our environment. Although, considerable progress has been achieved in the developments of GCN based photocatalysts, there are still many challenges to rationally design such a potential photocatalytic system towards better environmental pollution abatement. In order to address this challenge, further researches may be carried out in following directions.

Textural properties of a photoctalyst are crucial for an optimized optical and electronic structure and hence improved photocatalytic performance. Modification in the textural properties of GCN is essentially required to obtain an augmented photoactivity. For instant, ultrathin GCN nanosheets possess high specific surface area which facilitate to exhibit high photoactivity. Therefore, ultrathin GCN nanosheets have a great potential for the construction of advanced photocatalytic materials. However, GCN usually exhibit the poor specific surface area far below the theoretical value (2500 $m^2\ g^{-1}$). The band gap energy of GCN based materials needs further narrowing in order to harness energy from complete solar spectrum. Moreover, for efficient charge separation at the interface of the heterojunction, the close contact between GCN and the coupled semiconductor is required. This can be achieved through rational design in the preparation process. The surface property of GCN is required to be improved for better adsorption of reactants and construction of heterostructured

photocatalysts. Fine tuning of the surface properties at the atomic level might be a successful approach in achieving these aspects.

Acknowledgements The authors express sincere thanks to the management of S'O'A (Deemed to be university), Bhubaneswar for encouraging to carry out the present work.

References

1. R. Acharya, K. Parida, A review on TiO_2/g–C_3N_4 visible-light-responsive photocatalysts for sustainable energy generation and environmental remediation. J. Environ. Chem. Eng. **8**, 103896 (2020)
2. C. Zhai, M. Zhu, Y. Lu, F. Ren, C. Wang, Y. Du, P. Yang, Reduced graphene oxide modified highly ordered TiO_2 nanotube arrays photoelectrode with enhanced photoelectrocatalytic performance under visible-light irradiation. Phys. Chem. Chem. Phys. **16**(28), 14800 (2014)
3. V.K. Gupta, R. Kumar, A. Nayak, T.A. Saleh, M.A. Barakat, Adsorptive removal of dyes from aqueous solution onto carbon nanotubes: a review. Adv. Colloid Interf. Sci. **193**, 24–34 (2013)
4. Z. Jiang, H. Sun, T. Wang, B. Wang, W. Wei, H. Li, S. Yuan, T. An, H. Zhao, J. Yu, P.K. Wong, Nature-based catalyst for visible-light-driven photocatalytic CO_2 reduction, energy environ. Sci. **11**, 2382–2389 (2018)
5. R. Acharya, A. Lenka, K. Parida, Magnetite modified amino group based polymer nanocomposites towards efficient adsorptive detoxification of aqueous Cr (VI): a review. J. Mol. Liq. **337**, 116487 (2021)
6. T.X.H. Le, R. Esmilaire, M. Drobek, M. Bechelany, C. Vallicari, D.L. Nguyen, A. Julbe, S. Tingry, M. Cretin, Design of a novel fuel cell-Fenton system: a smart approach to zero energy depollution. J. Mater. Chem. A. **4**, 17686–17693 (2016)
7. R. Acharya, K. Parida, A review on adsorptive remediation of Cr (VI) by magnetic iron oxides and their modified form, 2020. Biointerf. Res. Appl. Chem. **10**, 5266–5272 (2020)
8. R. Acharya, K. Parida, Valorization of agricultural wastes as low-cost adsorbents towards efficient removal of aqueous Cr(VI), in: Shahid-ul-Islam, Shalla, A.H., Khan, S.A. (Eds.), *Handbook of Biomass Valorization for Industrial Applications*, John Wiley & Sons, pp. 507–530 (2022)
9. R. Acharya, S. Martha, K.M. Parida, Remediation of Cr (VI) using clay minerals, biomasses and industrial wastes as adsorbents, in Shahid-ul-Islam (ed.) *Advanced Materials for Wastewater Treatment*, Scrivener Publishing LLC, pp. 129–170 (2017)
10. R. Acharya, B. Naik, K.M. Parida, Adsorption of Cr (VI) and textile dyes on to mesoporous silica, titanate nanotubes and layer double hydroxides, in: Shahid ul-Islam, B.S. Butola (eds.) *Nanomaterials in the Wet Processing of Textiles*, John Wiley Scrivener USA, pp. 219–260 (2018)
11. M.V. Sofianou, M. Tassi, V. Psycharis, N. Boukos, S. Thanos, T. Vaimakis, J. Yu, C. Trapalis, Solvothermal synthesis and photocatalytic performance of Mn4+-doped anatase nanoplates with exposed 001 facets. Appl. Catal. B Environ. **162**, 27 (2015)
12. T.X.H. Le, M. Bechelany, J. Champavert, M. Cretin, A highly active based graphene cathode for the electro-fenton reaction. RSC Adv. **5**(53), 42536 (2015)
13. D.B. Miklos, C. Remy, M. Jekel, K.G. Linden, J.E. Drewes, U. Hubner, Evaluation of advanced oxidation processes for water and wastewater treatment—a critical review. Water Res. **139**, 118–131 (2018)
14. X. Jiang, M. Manawan, T. Feng, R. Qian, T. Zhao, G. Zhou, F. Kong, Q. Wang, S. Dai, J.H. Pan, Anatase and rutile in evonik aeroxide P25: heterojunctioned or individual nanoparticles? Catal. Today **300**(2018), 12–17 (2018)

15. S. Mansingh, S. Sultana, R. Acharya, M.K. Ghosh, K. Parida, Efficient Photon conversion via double charge dynamics CeO_2-$BiFeO_3$ p-n heterojunction photocatalyst promising toward N_2 fixation and Phenol-Cr (VI) detoxification. Inorg. Chem. **59**, 3856–3873 (2020)
16. S. Mansingh, R. Acharya, S. Martha, K.M. Parida, Pyrochlore $Ce_2Zr_2O_7$ decorated over rGO: a photocatalyst that proves to be efficient towards the reduction of 4-nitrophenol and degradation of ciprofloxacin under visible light. Phys. Chem. Chem. Phys. **20**, 9872–9885 (2018)
17. S. Mishra, R. Acharya, Photocatalytic applications of graphene based semiconductor composites: a review. Mater. Today Proceed. **35**(2021), 164–169 (2021)
18. R. Acharya, B. Naik, K.M. Parida, Cr(VI) remediation from aqueous environment through modified-TiO_2-mediated photocatalytic reduction, Beilstein. J. Nanotechnol. **9**, 1448–1470 (2018)
19. A. Fujishima, K. Honda, Electrochemical photolysis of water at a semiconductor electrode. Nature **238**(5358), 37 (1972)
20. J.H. Carey, J. Lawrence, H.M. Tosine, Photodechlorination of PCB's in the presence of titanium dioxide in aqueous suspensions Bull. Environ. Contam. Toxicol. **16**, 697–701 (1976)
21. M. Nasr, C. Eid, R. Habchi, P. Miele, M. Bechelany, Recent progress on TiO_2 nanomaterials for photocatalytic applications. Chem Sus Chem **11**, 3023–3047 (2018)
22. W. Zhang, H. He, H. Li, L. Duan, L. Zu, Y. Zhai, W. Li, L. Wang, H. Fu, D. Zhao, Visible-light responsive TiO_2-based materials for efficient solar energy utilization. Adv. Energy Mater. **11**, 2003303 (2021)
23. X.C. Wang, K. Maeda, A. Thomas, K. Takanabe, G. Xin, J.M. Carlsson, K. Domen, M. Antonietti, A metal-free polymeric photocatalyst for hydrogen production from water under visible light. Nat. Mater. **8**, 76–80 (2009)
24. G. Liao, Y. Gong, L. Zhang, H. Gao, G.-J. Yang, B. Fang, Semiconductor polymeric graphitic carbon nitride photocatalysts: the '"holy grail"' for the photocatalytic hydrogen evolution reaction under visible light, Energy Environ. Sci. **12**, 2080–2147 (2019)
25. S. Pati, R. Acharya, An overview on g-C_3N_4 as a robust photocatalyst towards the sustainable generation of H_2 energy. Mater. Today Proceed. **35**, 175–178 (2021)
26. S. Zhang, P. Gu, R. Ma, C. Luo, T. Wen, G. Zhao, W. Cheng, X. Wang, Recent developments in fabrication and structure regulation of visible-light driven g-C_3N_4-based photocatalysts towards water purification: a critical review. Catal. Today **335**, 65–77 (2019)
27. J. Wen, J. Xie, X. Chen, X. Li, A review on g-C_3N_4-based photocatalysts. Appl. Surf. Sci. **391**, 72–123 (2017)
28. W.-J. Ong, L.-L. Tan, Y.H. Ng, S.T. Yong, S.-P. Chai, Graphitic carbon nitride (g-C_3N_4)-based photocatalysts for artificial photosynthesis and environmental remediation: are we a step closer to achieving sustainability? Chem. Rev. **116**, 7159–7329 (2016)
29. Q. Zhang, X. Liu, M. Chaker, D. Ma, Advancing graphitic carbon nitride-based photocatalysts toward broadband solar energy harvesting. ACS Materials Lett. **3**, 663–697 (2021)
30. S. Sahoo, R. Acharya, An overview on recent developments in synthesis and molecular level structure of visible-light responsive g-C_3N_4 photocatalyst towards environmental remediation. Mater. Today Proceed. **35**, 150–155 (2021)
31. L. Acharya, B.P. Mishra, S.P. Pattnaik, R. Acharya, K. Parida, Incorporating nitrogen vacancies in exfoliated B-doped g-C_3N_4 towards improved photocatalytic ciprofloxacin degradation and hydrogen evolution. New. J. Chem. **46**, 3493–3503 (2022)
32. T. Su, Q. Shao, Z. Qin, Z. Guo, B. Wu, Role of interfaces in two-dimensional photocatalyst for water splitting. ACS Catal. **8**, 2253–2276 (2018)
33. R. Acharya, S. Pati, K. Parida, A review on visible light driven spinel ferrite-g-C_3N_4 photocatalytic systems with enhanced solar light utilization. J. Mol. Liq. **357**, 119105 (2022)
34. S. Yin, J. Han, T. Zhou, R. Xu, Recent progress in g-C_3N_4 based low cost photocatalytic system: activity enhancement and emerging applications. Catal. Sci. Technol. **5**, 5048–5061 (2015)
35. J. Fu, J. Yu, C. Jiang, B. Cheng, g-C_3N_4-based heterostructured photocatalysts. Adv. Energy Mater. **8**, 1701503 (2018)

36. J. Yang, H. Wang, L. Jiang, H. Yu, Y. Zhao, H. Chen, X. Yuan, L. Liang, H. Li, Z. Wu, Defective polymeric carbon nitride: Fabrications, photocatalytic applications and perspectives. Chem. Eng. J. **427**, 130991 (2022)
37. A. Naseri, M. Samadi, A. Pourjavadi, A.Z. Moshfegh, S. Ramakrishna, Graphitic carbon nitride ($g\text{-}C_3N_4$)-based photocatalysts for solar hydrogen generation: recent advances and future development directions. J. Mater. Chem. A. **5**, 23406 (2017)
38. X. Li, J. Yu, M. Jaroniec, Hierarchical photocatalysts. Chem. Soc. Rev. **45**, 2603–2636 (2016)
39. X. Li, J. Yu, J. Low, Y. Fang, J. Xiao, X. Chen, Engineering heterogeneous semiconductors for solar water splitting. J. Mater. Chem. A. **3**, 2485–2534 (2015)
40. R. Acharya, L. Acharya, K. Parida, $BiFeO_3$-based materials for augmented photoactivity, Khursheed Ahmad and Waseem Raza (eds.) Perovskite Materials for Energy and Environmental Applications, John Wiley & Sons, Inc. p167–217 (2022)
41. S. Borthakur, L. Saikia, $ZnFe_2O_4$@$g\text{-}C_3N_4$ nanocomposites: an efficient catalyst for Fenton-like photodegradation of environmentally pollutant Rhodamine B. J. Environ. Chem. Eng. **7**, 103035 (2019)
42. S. Kim, K.H. Kim, C. Oh, K. Zhang, J.H. Park, Artificial photosynthesis for high-value-added chemicals: Old material, new opportunity. Carbon Energy **4**, 21–44 (2022)
43. W. Zhang, L. Li, Y. Gao, D. Zhang, Graphitic carbon nitride-based materials for photocatalytic reduction of U(VI), New. J. Chem. **44**, 19961–19976 (2020)
44. Y. Wang, Y. Zhang, T.C. Zhang, G. Xiang, C. Wang, S. Yuan, Removal of trace arsenite through simultaneous photocatalytic oxidation and adsorption by magnetic Fe_3O_4@PpPDA@TiO_2 core–shell nanoparticles. ACS Appl. Nano Mater. **3**, 8495–8504 (2020)
45. J. Feng, L. Peng, C. Wu, X. Sun, S. Hu, C. Lin, J. Dai, J. Yang, Y. Xie, Giant moisture responsiveness of VS_2 ultrathin nanosheets for novel touchless positioning interface. Adv. Mater. **24**, 1969–1974 (2012)
46. G. Eda, T. Fujita, H. Yamaguchi, D. Voiry, M.W. Chen, M. Chhowalla, Coherent atomic and electronic heterostructures of single-layer MoS_2. ACS Nano **22**, 7311 (2012)
47. Y. Omomo, T. Sasaki, L.Z. Wang, M. Watanabe, Redoxable nanosheet crystallites of MnO_2 derived via delamination of a layered manganese oxide. J. Am. Chem. Soc. **125**, 3568 (2003)
48. S. Ithurria, M.D. Tessier, B. Mahler, R.P.S.M. Lobo, B. Dubertret, A.L. Efros, Colloidal nanoplatelets with two-dimensional electronic structure. Nat. Mater. **10**, 936 (2011)
49. A.K. Geim, K.S. Novoselov, The rise of graphene. Nat. Mater. **6**, 183–191 (2007)
50. H. Zhang, Ultrathin two-dimensional nanomaterials. ACS Nano **9**, 9451 (2015)
51. P. Xia, B. Zhu, J. Yu, S. Cao, M. Jaronie, Ultra-thin nanosheet assemblies of graphitic carbon nitride for enhanced photocatalytic CO_2 reduction. J. Mater. Chem. A. **5**, 3230 (2017)
52. J. Yang, Z. Chen, N. Mao, D. An, B.D. Wang, Fahlman, Ultrathin $g\text{-}C_3N_4$ nanosheets with an extended visible-light-responsive range for significant enhancement of photocatalysis. RSC Adv. **7**, 2333 (2017)
53. P. Niu, L. Zhang, G. Liu, H.-M. Cheng, Graphene-like carbon nitride nanosheets for improved photocatalytic activities. Adv. Funct. Mater. **22**, 4763 (2012)
54. F. Dong, Y. Li, Z. Wang, W.-K. Ho, Enhanced visible light photocatalytic activity and oxidation ability of porous graphene-like $g\text{-}C_3N_4$ nanosheets via thermal exfoliation. Appl. Surf. Sci. **358**, 393–403 (2015)
55. K. Schwinghammer, M.B. Mesch, V. Duppel, C. Ziegler, J. Senker, B.V. Lotsch, Crystalline carbon nitride nanosheets for improved visible-light hydrogen evolution. J. Am. Chem. Soc. **136**, 1730 (2014)
56. V. Nicolosi, M. Chhowalla, M.G. Kanatzidis, M.S. Strano, J.N. Coleman, Liquid exfoliation of layered materials. Science **340**, 1226419 (2013)
57. J.N. Coleman, M. Lotya, A. O'Neill, S.D. Bergin, P.J. King, U. Khan, K. Young, A. Gaucher, S. De, R.J. Smith, I.V. Shvets, S.K. Arora, G. Stanton, H.Y. Kim, K. Lee, G.T. Kim, G.S. Duesberg, T. Hallam, J.J. Boland, J.J. Wang, J.F. Donegan, J.C. Grunlan, G. Moriarty, A. Shmeliov, R.J. Nicholls, J.M. Perkins, E.M. Grieveson, K. Theuwissen, D.W. McComb, P.D. Nellist, V. Nicolosi, Two-dimensional nanosheets produced by liquid exfoliation of layered materials science **331**, 568 (2011)

58. S. Yang, Y. Gong, J. Zhang, L. Zhan, L. Ma, Z. Fang, R. Vajtai, X. Wang, P.M. Ajayan, Exfoliated graphitic carbon nitride nanosheets as efficient catalysts for hydrogen evolution under visible light. Adv. Mater. **25**, 2452–2456 (2013)
59. D.R. Dreyer, S. Park, C.W. Bielawski, R.S. Ruoff, The chemistry of graphene oxide. Chem. Soc. Rev. **39**, 228 (2010)
60. J.H. Lee, M.J. Park, S.J. Yoo, J.H. Jang, H.J. Kim, S.W. Nam, C.W. Yoon, J.Y. Kim, A highly active and durable Co–N–C electrocatalyst synthesized using exfoliated graphitic carbon nitride nanosheet Nanoscale **7**, 10334 (2015)
61. J. Xu, L. Zhang, R. Shi, Y. Zhu, Chemical exfoliation of graphitic carbon nitride for efficient heterogeneous photocatalysis. J. Mater. Chem. A. **1**, 14766 (2013)
62. F. Cheng, H. Wang, X. Dong, The amphoteric properties of g-C_3N_4 nanosheets and fabrication of their relevant heterostructure photocatalysts by an electrostatic re-assembly route. Chem. Commun. **51**, 7176 (2015)
63. S.P. Pattnaik, A. Behera, S. Martha, R. Acharya, K. Parida, Facile synthesis of exfoliated graphitic carbon nitride for photocatalytic Degradation of ciprofloxacin under solar irradiation. J. Mater. Sci. **54**, 5726–5742 (2019)
64. S.P. Pattnaik, A. Behera, R. Acharya, K. Parida, Green exfoliation of graphitic carbon nitride towards decolourization of congo-red under solar irradiation. J. Environ. Chem. Eng. **7**, 103456 (2019)
65. Y. Fang, I.S. Merenkov, X. Li, J. Xu, S. Lin, M.L. Kosinova, X. Wang, Vertically aligned 2D carbon doped boron nitride nanofilms for photoelectrochemical water oxidation. J. Mat. Chem. **8**, 13059–13064 (2020)
66. L. Acharya, S.P. Pattnaik, A. Behera, R. Acharya, K. Parida, Exfoliated boron nitride (e-BN) tailored exfoliated graphitic carbon nitride (e-CN): an improved visible light mediated photocatalytic approach towards TCH degradation and H2 evolution. Inorg. Chem. **60**, 5021–5033 (2021)
67. B.P. Mishra, K. Parida, Orienting Z scheme charge transfer in graphitic carbon nitride-based systems for photocatalytic energy and environmental applications. J. Mat. Chem. A. **9**, 10039–10080 (2021)
68. S. Patnaik, D.P. Sahoo, K. Parida, Recent advances in anion doped g-C_3N_4 photocatalysts: a review. Carbon **172**, 682–711 (2021)
69. M.S. Khan, F. Zhang, M. Osada, S.S. Mao, S. Shen, Graphitic carbon nitride-based low-dimensional heterostructures for photocatalytic applications. Solar RRL **4**, 1900435 (2020)
70. X. Dong, F. Cheng, Recent development in exfoliated two-dimensional g-C_3N_4 nanosheets for photocatalytic applications. J. Mat. Chem. A. **3**, 23642–23652 (2015)
71. L. Ke, P. Li, X. Wu, S. Jiang, M. Luo, Y. Liu, Z. Le, C. Sun, S. Song, Graphene-like sulfur-doped g-C_3N_4 for photocatalytic reduction elimination of UO_2^{2+} under visible Light. Appl. Catal. B: Environmental. **205**, 319–326 (2017)
72. X. Liu, R. Ma, L. Zhuang, B. Hu, J. Chen, X. Liu, X. Wang, Recent developments of doped g-C_3N_4 photocatalysts for the degradation of organic pollutants. Crit. Rev. Environ. Sci. Technol. **51**, 751–790 (2021)
73. L. Jiang, X. Yuan, Y. Pan, J. Liang, G. Zeng, Z. Wu, H. Wang, Doping of graphitic carbon nitride for photocatalysis: a reveiw. Appl. Catal. B: Environmental **217**, 388–406 (2017)
74. Y. Zhou, W. Lv, B. Zhu, F. Tong, J. Pan, J. Bai, Q. Zhou, H. Qin, Template-free one-step synthesis of g-C_3N_4 nanosheets with simultaneous porous network and S-doping for remarkable visible-light-driven hydrogen evolution. ACS Sustain. Chem. Eng. **7**, 5801–5807 (2019)
75. L. Acharya, G. Swain, B.P. Mishra, R. Acharya, K. Parida, Development of $MgIn_2S_4$ microflower-embedded exfoliated B-Doped g-C_3N_4 nanosheets: p–n heterojunction photocatalysts toward photocatalytic water reduction and H_2O_2 production under visible-light irradiation. ACS Appl. Energy Mater. **5**, 2838–2852 (2022)
76. F. He, Z. Wang, Y. Li, S. Peng, B. Liu, The nonmetal modulation of composition and morphology of g-C_3N_4 -based photocatalysts. Appl. Catal. B: Environ. **269**, 118828 (2020)

77. S. Tonda, S. Kumar, S. Kandula, V. Shanker, Fe-doped and-mediated graphitic carbon nitride nanosheets for enhanced photocatalytic performance under natural sunlight. J. Mat. Chem. A. **2**, 6772–6780 (2014)
78. J. Gao, Y. Wang, S. Zhou, W. Lin, Y. Kong, A facile one-step synthesis of Fe-doped g-C_3N_4 nanosheets and their improved visible-light photocatalytic performance. ChemCatChem **9**, 1708–1715 (2017)
79. S. Hu, F. Li, Z. Fan, F. Wang, Y. Zhao, Z. Lv, Band gap-tunable potassium doped graphitic carbon nitride with enhanced mineralization ability. Dalton Trans. **44**, 1084–1092 (2015)
80. P. Chen, P. Xing, Z. Chen, H. Lin, Y. He, Rapid and energy-efficient preparation of boron doped g-C_3N_4 with excellent performance in photocatalytic H_2-evolution. Int. J. Hydrog. Energy. **43**, 19984–19989 (2018)
81. Y.R. Lin, G.V.C. Dizon, K. Yamada, C.Y. Liu, A. Venault, H.Y. Lin, M. Yoshida, C. Hu, Sulfur-doped g-C_3N_4 nanosheets for photocatalysis: Z-scheme water splitting and decreased biofouling. J. Colloid Interface Sci. **567**, 202–212 (2020)
82. Y. Deng, L. Tang, G. Zeng, Z. Zhu, M. Yan, Y. Zhou, J. Wang, Y. Liu, J. Wang, Insight into highly efficient simultaneous photocatalytic removal of Cr (VI) and 2, 4-diclorophenol under visible light irradiation by phosphorus doped porous ultrathin g-C_3N_4 nanosheets from aqueous media: performance and reaction mechanism. Appl. Catal. B: Environ. **203**, 343–354 (2017)
83. J. Gao, J. Wang, X. Qian, Y. Dong, H. Xu, R. Song, C. Yan, H. Zhu, Q. Zhong, G. Qian, J. Yao, One-pot synthesis of copper-doped graphitic carbon nitride nanosheet by heating Cu–melamine supramolecular network and its enhanced visible-light-driven photocatalysis. J. Solid State Chem. **228**, 60–64 (2015)
84. Y. Zhou, L. Zhang, W. Huang, Q. Kong, X. Fan, M. Wang, J. Shi, N-doped graphitic carbon-incorporated g-C_3N_4 for remarkably enhanced potocatalytic H_2 evolution under visible light. Carbon **99**, 111–117 (2016)
85. Y. Wang, S. Zhao, W. Zhang, J. Fang, Y. Zhou, S. Yuan, One-pot synthesis of K-doped g-C_3N_4 nanosheets with enhanced photocatalytic hydrogen production under visible-light irradiation. Appl. Surf. Sci. **440**, 258–265 (2018)
86. L. Acharya, S. Nayak, S.P. Pattnaik, R. Acharya, K. Parida, Resurrection of boron nitride in p-n type-II boron nitride/B-doped-g-C_3N_4 nanocomposite during solid-state Z-scheme charge transfer path for the degradation of tetracycline hydrochloride. J. Colloid Interface Sci. **566**, 211–223 (2020)
87. J. Zhang, S. Hu, Y. Wang, A convenient method to prepare a novel alkali metal sodium doped carbon nitride photocatalyst with a tunable band structure. RSC adv. **4**, 62912–62919 (2014)
88. G. Mamba, A.K. Mishra, Graphitic carbon nitride (g-C_3N_4) nanocomposites: a new and exciting generation of visible light driven photocatalysts for environmental pollution remediation. Appl. Catal. B. **198**, 347 (2016)
89. N. Tian, H.W. Huang, X. Du, F. Dong, Y.H. Zhang, , Rational nanostructure design of graphitic carbon nitride for photocatalytic applications. J. Mater. Chem. A **7**, 11584–11612 (2019)
90. Q.L. Xu, L.Y. Zhang, J.G. Yu, S. Wageh, A.A. Al-Ghamdi, M. Jaroniec, Direct Z-scheme photocatalysts: principles, synthesis, and applications. Mater. Today **21**, 1042–1063 (2018)
91. P. Zhou, J.G. Yu, M. Jaroniec, All-solid-state Z-scheme photocatalytic systems. Adv. Mater. **26**, 4920–4935 (2014)
92. H. Yang, A short review on heterojunction photocatalysts: Carrier transfer behavior and photocatalytic mechanisms. Mater. Res. Bull. **142**, 111406 (2021)
93. M. Shim, M. McDaniel, N. Oh, Prospects for strained type-II nanorod heterostructures. J. Phys. Chem. Lett. **2**, 2722–2727 (2011)
94. H. McDaniel, P.E. Heil, C.L. Tsai, K.K. Kim, M. Shim, Integration of type II nanorod heterostructures into photovoltaics. ACS Nano **5**, 7677–7683 (2011)
95. H. Wang, L. Zhang, Z. Chen, J. Hu, S. Li, Z. Wang, J. Liu, X. Wang, Semiconductor heterojunction photocatalysts: design, construction, and photocatalytic performances. Chem. Soc. Rev. **43**, 5234 (2014)

96. Z. Zhao, Y. Sun, F. Dong, Graphitic carbon nitride based nanocomposites: a review. Nanoscale **7**, 15–37 (2015)
97. X. Li, M. Edelmannová, P. Huo, K. Kočí, Fabrication of highly stable CdS/g-C3N4 composite for enhanced photocatalytic degradation of RhB and reduction of CO_2. J Mater Sci **55**, 3299–3313 (2020)
98. D.R. Paul, S. Gautam, P. Panchal, S.P. Nehra, P. Choudhary, A. Sharma, ZnO-Modified g-C_3N_4: a potential photocatalyst for environmental application. ACS Omega **5**, 3828–3838 (2020)
99. I. Ali, J.-O. Kim, Optimization of photocatalytic performance of a gC_3N_4–TiO2 nanocomposite for phenol degradation in visible light. Mat. Chem. Phys. **261**, 124246 (2021)
100. R. He, K. Cheng, Z. Wei, S. Zhang, D. Xu, Room-temperature in situ fabrication and enhanced photocatalytic activity of direct Z-scheme BiOI/g-C_3N_4 photocatalyst. Appl. Surf. Sci. **465**, 964–972 (2019)
101. J. Li, Y. Liu, C. Chen, Fabrication of gC_3N_4/TiO_2 composite photocatalyst with extended absorption wavelength range and enhanced photocatalytic performance. J. Photochem. Photobiol. A : Chem. **317**, 151–160 (2016)
102. T. Sheng, Z. Wei, H. Miao, W. Yao, H. Li, Y. Zhu, Enhanced organic pollutant photodegradation via adsorption/photocatalysis synergy using a 3D gC_3N_4/TiO_2 free separation photocatalyst. Chem. Eng. J. **370**, 287–294 (2019)
103. Y. Tian, B. Chang, J. Fu, B. Zhou, J. Liu, F. Xi, X. Dong, J., Graphitic carbon nitride/Cu_2O heterojunctions: Preparation, characterization, and enhanced photocatalytic activity under visible light. Solid State Chem. **212**, 1 (2014)
104. J. Fu, Q. Xu, J. Low, C. Jiang, J. Yu, Ultrathin 2D/2D WO_3/g-C_3N_4 step-scheme H_2-production photocatalyst. Appl. Catal. B: Environ. **243**, 556–565 (2019)
105. Y. Zhen, C. Yang, F. Fu, H. Shen, W. Xue, C. Gu, J. Feng, Y. Zhang, Y. Liang, Photocatalytic performance and mechanism insights of S-scheme g-C_3N_4/Bi_2MoO_6 heterostructure in phenol degradation and hydrogen evolution reaction under visible light. Phys. Chem. Chem. Phys. **22**, 26278–26288 (2020)
106. K.N. Van, H.T. Huu, V.N.N. Thi, T.L.L. Thi, D.H. Truong, Ts.T. Truong, N.N. Dao, V. Vo, D.L. Tran, Y. Vasseghian, Facile construction of S-scheme SnO_2/g-C_3N_4 photocatalyst for improved photoactivity. Chemosphere **289**, 133120 (2022)
107. S. Mishra, R. Acharya, K. Parida, Spinel-ferrite-decorated graphene-based nanocomposites for enhanced photocatalytic detoxification of organic dyes in aqueous medium: a review. Water **15**(1), 81 (2023)
108. M. Faisala, M. Jalalaha, F.A. Harraza, A.M. El-Tonic, A. Khan, M.S. Al-Assiri, Au nanoparticles-doped g-C3N4 nanocomposites for enhanced photocatalytic performance under visible light illumination. Ceram. Int. **46**, 22090–22101 (2020)
109. S.C. Yan, Z.S. Li, Z.G. Zou, Photodegradation of rhodamine B and methylorange over boron-doped g-C_3N_4 under visible light irradiation. Langmuir **26**, 3894–3901 (2010)
110. W. Gu, F. Lu, C. Wang, S. Kuga, L.-Z. Wu, Y. Huang, M. Wu, Face-to-Face interfacial assembly of ultrathin g-C_3N_4 and anatase TiO_2 nanosheets for enhanced solar photocatalytic activity, ACS Appl. Mater. Interfaces. **9**, 28674–28684 (2017)
111. L. Wang, Y. Li, P. Han, Electrospinning preparation of g-C_3N_4/Nb_2O_5 nanofibers heterojunction for enhanced photocatalytic degradation of organic pollutants in water. Sci. Rep. **11**, 22950 (2021)
112. V. Kumaravel, J. Bartlett, S.C. Pillai, Photoelectrochemical conversion of carbon dioxide (CO_2) into fuels and value-added products. ACS Energy Lett. **5**, 486–519 (2020)
113. I. Masood ul Hasan, L. Peng, J. Mao, R. He, Y. Wang, J. Fu, N. Xu, J. Qiao, Carbon-based metalfree catalysts for electrochemical CO_2 reduction: activity, selectivity, and stability. Carbon Energy **3**, 24–49
114. X. Chang, T. Wang, J. Gong, CO_2 photo-reduction: insights into CO_2 activation and reaction on surfaces of photocatalysts. Energy Environ. Sci. **9**, 2177–2196 (2016)
115. Y. Shioya, K. Ikeue, M. Ogawa, M. Anpo, synthesis of transparent Ti-containing mesoporous silica thin film materials and their unique photocatalytic activity for the reduction of CO_2 with H_2O. Appl Catal A-Gen. **254**, 251–259 (2003)

116. A. Hasani, M.A. Teklagne, H.H. Do, S.H. Hong, Q.V. Le, S.H. Ahn, S.Y. Kim, Graphene-based catalysts for electrochemical carbon dioxide reduction. Carbon Energy. **2**, 158–175 (2020)
117. D. Chen, Y. Wang, D. Liu, H. Liu, C. Qian, H. He, J. Yang, Surface composition dominates the electrocatalytic reduction of CO_2 on ultrafine CuPd nanoalloys. Carbon Energy. **2**, 443–451 (2020)
118. E.V. Kondratenko, G. Mul, J. Baltrusaitis, G.O. Larrazábal, J. Pérez-Ramírez, Status and perspectives of CO_2 conversion into fuels and chemicals bycatalytic, photocatalytic and electrocatalytic processes. Energy Environ. Sci. **6**, 3112–3135 (2013)
119. W. Dai, H. Xu, J. Yu, X. Hu, X. Luo, X. Tu, L. Yang, Photocatalytic reduction of CO_2 into methanol and ethanol over conducting polymers modified Bi_2WO_6 microspheres under visible light. Appl. Surf. Sci. **356**, 173–180 (2015)
120. S.W. Jo, B.S. Kwak, K.M. Kim, J.Y. Do, N.-K. Park, S.O. Ryu, H.-J. Ryu, J.-I. Baek, M. Kang, Effectively CO_2 photoreduction to CH_4 by the synergistic effects of Ca and Ti on Ca-loaded TiSiMCM-41 mesoporous photocatalytic systems. Appl. Surf. Sci. **355**, 891–901 (2015)
121. M. Halmann, Photoelectrochemical reduction of aqueous carbon dioxide on p-type gallium phosphide in liquid junction solar cells. Nature **275**, 115–116 (1978)
122. W. Jiang, X. Yin, F. Xin, Y. Bi, Y. Liu, X. Li, Preparation of $CdIn_2S_4$ microspheres and application for photocatalytic reduction of carbondioxide. Appl. Surf. Sci. **288**, 138–142 (2014)
123. Y.-X. Pan, Z.-Q. Sun, H.-P. Cong, Y.-L. Men, S. Xin, J. Song, S.-H. Yu, Photocatalytic CO_2 reduction highly enhanced by oxygen vacancies on Pt-nanoparticle-dispersed gallium oxide. Nano Res. **9**, 1689–1700 (2016)
124. P. Li, H. Xu, L. Liu, T. Kako, N. Umezawa, H. Abe, J. Ye, Constructing cubic-orthorhombic surface-phase junctions of $NaNbO_3$ towards significant enhancement of CO_2 photoreduction. J. Mater. Chem. A. **2**, 5606–5609 (2014)
125. Y. Jia, H. Ma, W. Zhang, G. Zhu, W. Yang, N. Son, M. Kang, C. Liu, Z-scheme $SnFe_2O_4$-graphitic carbon nitride: reusable, magnetic catalysts for enhanced photocatalytic CO_2 reduction. Chem. Eng. J. **383**, 123172 (2020)
126. X. Li, J. Yu, M. Jaroniec, X. Chen, Cocatalysts for selective photoreduction of CO_2 into solar fuels. Chem. Rev. **119**, 3962–4179 (2019)
127. Q. Zhang, C.F. Lin, B.Y. Chen, T. Ouyang, C.T. Chang, Deciphering visible light photoreductive conversion of CO_2 to formic acid and methanol using waste prepared material. Environ. Sci. Technol. **49**, 2405–2417 (2015)
128. M. Li, L. Zhang, X. Fan, Y. Zhou, M. Wu, J. Shi, Highly selective CO_2 photoreduction to CO over g-C_3N_4/Bi_2WO_6 composites under visible light. J Mater Chem A. **3**, 5189–5196 (2015)
129. K. Sonowal, N. Nandal, P. Basyach, L. Kalita, S.L. Jain, L. Saikia, Photocatalytic reduction of CO_2 to methanol using Zr (IV)-based MOF composite with g-C_3N_4 quantum dots under visible light irradiation. J. CO2 Utiliz **57**, 101905 (2022)
130. Y. Zou, X. Wang, A. Khan, P. Wang, Y. Liu, A. Alsaedi, T. Hayat, X. Wang, Environmental remediation and application of nanoscale zero-valent iron and its composites for the removal of heavy metal ions: a review environ. Sci. Technol. **50**, 7290–7304 (2016)
131. C. Chen, Z. Chai, X. Wang, Metal–organic framework-based materials: superior adsorbents for the capture of toxic and radioactive metal ions. Chem. Soc. Rev. **47**, 2322–2356 (2018)
132. Z. Zhang, C. Liu, Z. Dong, Y. Dai, G. Xiong, Y. Liu, Y. Wang, Y. Wang, Y. Liu, synthesis of flower-like MoS_2/g-C_3N_4 nanosheet heterojunctions with enhanced photocatalytic reduction activity of uranium(VI) Appl. Surf. Sci. **520**, 146352 (2020)
133. R. Acharya, P. Pani, Visible light susceptible doped TiO2 photocatalytic systems: an overview. Mater. Today: Proc. **67**, 1276–1282 (2022)
134. S.P. Tripathy, S. Subudhi, R. Acharya, R. Acharya, M. Das, K.M. Parida, Adsorptive removal of Cr (VI) onto UiO-66-NH_2 and its determination by radioanalytical techniques. J. Radioanal. Nucl. Chem. **322**, 983–992 (2019)
135. M. Wang, Y. Zeng, G. Dong, C. Wang, Br doping of g-C_3N_4 towards enhanced photocatalytic performance in Cr (VI) reduction, Chinese. J. Catal. **41**, 1498–1510 (2020)

136. Y. Wang, S. Bao, Y. Liu, W. Yang, Y. Yu, M. Feng, K. Li, Efficient photocatalytic reduction of Cr(VI) in aqueous solution over CoS_2/g-C_3N_4-rGO nanocomposites under visible light. Appl. Surf. Sci. **510**, 145495 (2020)
137. Y.H. Wang, M. Frutschi, E. Suvorova, V. Phrommavanh, M. Descostes, A.A.A. Osman, G. Geipel, L.R. Bernier-, Mobile uranium(IV)-bearing colloids in a mining-impacted wetland. Nat. Commun. **4**, 2942–2950 (2013)
138. Z. Huang, Z. Li, Q. Wu, L. Zheng, L. Zhou, Z. Chai, X. Wang, W. Shi, Simultaneous elimination of cationic uranium(vi) and anionic rhenium(vii) by graphene oxide–poly(ethyleneimine) macrostructures: a batch, XPS, EXAFS, and DFT combined study, Environ. Sci. Nano. **5**, 2077–2087 (2018)
139. S. Lee, U. Kang, G. Piao, S. Kim, D.S. Han, H. Park, Homogeneous photoconversion of seawater uranium using copper and iron mixed-oxide semiconductor electrodes. Appl. Catal. B. **207**, 35–41 (2017)
140. G. Wang, J. Zhen, L. Zhou, F. Wu, N. Deng, Adsorption and photocatalytic reduction of U (VI) in aqueous TiO_2 suspensions enhanced with sodium formate. J. Radioanal. Nucl. Chem. **304**, 579–585 (2015)
141. S. Tripathi, R. Bose, A. Roy, S. Nair, S. Ravishankar, Synthesis of hollow nanotubes of Zn_2SiO_4 or SiO_2: mechanistic understanding and uranium adsorption behaviour. ACS Appl. Mater. Interfaces. **7**, 26430–26436.
142. C. Lu, R. Chen, X. Wu, M. Fan, Y. Liu, Z. Le, S. Jiang, S. Song, Boron doped g-C_3N_4 with enhanced photocatalytic UO_2^{2+} reduction performance. Appl. Surf. Sci. **360**, 1016–1022 (2016)
143. C. Lu, P. Zhang, S. Jiang, X. Wu, S. Song, M. Zhu, Z. Lou, Z. Li, F. Liu, Y. Liu, Y. Wang, Z. Le, Photocatalytic reduction elimination of UO_2^{2+} pollutant under visible light with metal-free sulfur doped g-C_3N_4 photocatalyst. Appl. Catal. B. **200**, 378–385 (2017)
144. X. Jiang, Q. Xing, X. Luo, F. Li, J. Zou, S. Liu, X. Lia, X. Wang, Simultaneous photoreduction of Uranium(VI) and photooxidation of Arsenic(III) in aqueous solution over g-C_3N_4/TiO_2 heterostructured catalysts under simulated sunlight irradiation. Appl. Catal. B. **228**, 29–38 (2018)
145. Y. Wang, X.M. Liu, Q.I. Chen, T.C. Zhang, L. Ouyang, S.J. Yuan, Simultaneous photocatalytic oxidation and adsorption for efficient As(III) removal by magnetic BiOI/γ-Fe_2O_3 core-shell nanoparticles. Mater. Today Chem. **24**, 100823 (2022)
146. M.N. Maga˜na, A.E. Gonz´alez, L.M. Ix, S.C. Díaz, R. G´omez, Improved photocatalytic oxidation of arsenic (III) with WO_3/TiO_2 nanomaterials synthesized by the sol-gel method. J. Environ. Manag. **282**, 111602 (2021)
147. H. Eslami, M.H. Ehrampoush, A. Esmaeili, A.A. Ebrahimi, M.H. Salmani, M.T. Ghaneian, H. Falahzadeh, Efficient photocatalytic oxidation of arsenite from contaminated water by Fe_2O_3-Mn_2O_3 nanocomposite under UVA radiation and process optimization with experimental design. Chemosphere **207**, 303–312 (2018)
148. W. Ali, N. Mushtaq, T. Javed, H. Zhang, K. Ali, A. Rasool, A. Farooqi, Vertical mixing with return irrigation water the cause of arsenic enrichment in groundwater of district Larkana Sindh, Pakistan. Environ. Pollut. **245**, 77–88 (2019)
149. A.S. Maghsoudi, S. Hassani, K. Mirnia, M. Abdollahi, Recent advances in nanotechnology-based biosensors development for detection of arsenic, lead, mercury, and cadmium. Int. J. Nanomed. **16**, 803–832 (2021)
150. S.-Y. Yu, Y. Liu, H.-T. Ren, Z.-Y. Liu, X. Han, Importance of the ligand-to-metal charge transfer (LMCT) pathway in the photocatalytic oxidation of arsenite by TiO_2. Phys. Chem. Chem. Phys. **24**, 13661–13670 (2022)
151. M. Xiao, R. Li, J. Yin, J. Yang, X. Hu, H. Xiao, W. Wang, T. Yang, Enhanced photocatalytic oxidation of As(III) by TiO_2 modified with Fe_3O_4 through Ti-O-Fe interface bonds. Colloids Surf., A **651**, 129678 (2022)
152. L. Ouyang, Y. Zhang, Y. Wang, X. Wang, S. Yuan, Insights into the adsorption and photocatalytic oxidation behaviors of boron-doped TiO_2/gC_3N_4 nanocomposites toward As(III) in aqueous solution. Ind. Eng. Chem. Res. **60**, 7003–7013 (2021)

153. C. Wang, Y. Dai, X. Fu, X. Lu, J. Zhang, A novel layer-layer crossed structure of bentonite/g-C_3N_4 for enhanced photocatalytic oxidation of arsenic (III) in a wide pH range. Surf. Interf. **26**, 101365 (2021)
154. X. Wang, S.O. Pehkonen, A.K. Ray, Photocatalytic reduction of Hg(II) on two commercial TiO_2 catalysts. Electrochim. Acta **49**, 1435–1444 (2004)
155. K. Sundseth, J. Pacyna, E. Pacyna, N. Pirrone, R. Thorne, Global sources and pathways of mercury in the context of human health. Int. J. Environ. Res. Publ. Health **14**, 105–119 (2017)
156. Y. Fu, J. Jiang, Z. Chen, S. Ying, J. Wang, J. Hu, Rapid and selective removal of Hg (II) ions and high catalytic performance of the spent adsorbent based on functionalized mesoporous silica/poly (m-aminothiophenol) nanocomposite. J. Mol. Liq. **286**, 110746 (2019)
157. Y. Li, M. Xia, F. An, N. Ma, X. Jiang, S. Zhu, D. Wang, J. Ma, Superior removal of Hg (II) ions from wastewater using hierarchically porous, functionalized carbon. J. Hazard. Mater. **371**, 33–41 (2019)
158. G.G. Lenzi, C.V.B. Fávero, L.M.S. Colpini, H. Bernabe, M.L. Baesso, S. Specchia, O.A.A. Santos, Photocatalytic reduction of Hg(II) on TiO_2 and Ag/TiO_2 prepared by the sol–gel and impregnation methods. Desalination **270**, 241–247 (2011)
159. H. Alshaikh, A. Shawky, L.S. Roselin, Promoted visible-light photocatalytic reduction of Hg^{2+} over $CuAl_2O_4$-decorated g-C_3N_4 nanoheterojunctions synthesized by solution process. J. Env. Chem. Eng. **9**, 106778 (2021)
160. R.M. Mohamed, A.A. Ismail, Mesoporous $BiVO_4$/2D-g-C_3N_4 heterostructures for superior visible light-driven photocatalytic reduction of Hg (II) ions. Ceram. Intern. **47**, 26063–26073 (2021)